Nonlinear waves in pantographic beams induced by transverse impulses

Emilio Turco, Emilio Barchiesi, Alessandro Ciallella, Francesco Dell'isola

Nonlinear waves in pantographic beams induced by transverse impulses

Emilio Turco [a,*], Emilio Barchiesi [a,b], Alessandro Ciallella [c], Francesco dell'Isola [d]

[a] Department of Architecture, Design and Urban planning (DADU), University of Sassari, Italy
[b] Universidad de Lima, Instituto de Investigación Científica, Av. Javier Prado Este 4600, Santiago de Surco 15023, Peru
[c] International Research Center on Mathematics and Mechanics of Complex Systems (M&MOCS), University of L'Aquila, Italy
[d] Department of Civil, Construction-Architectural and Environmental Engineering (DICEAA), University of L'Aquila, Italy

A B S T R A C T

We present and discuss the results of some numerical simulations dealing with wave motion in one-dimensional pantographic media, also known as pantographic beams. Specifically, the analysis is carried out in large displacements regime and pantographic beams are modeled by using a completely discrete approach. Nonlinear vibrations induced by a transversal impulse are studied. A simple yet efficient time-stepping scheme was used to reconstruct the motion and, consequently, to explore the propagation of strain waves in the pantographic medium. The numerical study concludes that the main features of the observed strain wave propagation are extremely useful toward the understanding of the dynamic behavior of the pantographic micro-structure and its continuum counterparts.

Keywords:
Mechanics of metamaterials
Discrete models
Nonlinear waves
Stepwise time analysis

1. Introduction

The present paper continues the investigation started in the work [1]. Specifically, a strip of pantographic fabrics is considered. Pantographic materials [2,3], in their initial conception, were actually fabrics consisting of two orthogonal families of parallel equispaced bending elements, *i.e.* beams/fibers, connected at their intersection points through possibly elastic hinges. With regard to their physical realization, pantographic fabrics were designed in such a way that the two families of beams lie onto two different parallel planes and are connected by cylindrical pivots acting ideally as in-plane elastic hinges, *i.e.* hinges with torsional springs [4,5]. Actually, the behavior of these cylindrical pivots has been proven to be more complex and to involve in large deformation significant non-torsional deformation modes. Considering a full three-dimensional environment, also beams have proven to not move in-plane even when problems with in-plane boundary conditions are considered [6,7]. Local and non-local buckling phenomena have also been reported in the literature [8,9].

Many variations and enhancements of the design of pantographic fabrics were proposed in the literature in the last five years, including the introduction of perfect, *i.e.* non-elastic, hinges [10,11]. Furthermore, non-orthogonal families of fibers [12], as well as non-straight fibers [13], have been considered. Undoubtedly, the physical realization of pantographic materials has stimulated many studies addressing challenging issues not only in mechanics, but also in

* Corresponding author.
E-mail addresses: emilio.turco@uniss.it (E. Turco), emilio.barchiesi@uniss.it (E. Barchiesi), ale.ciallella@gmail.com (A. Ciallella), francesco.dellisola@univaq.it (F. dell'Isola).

additive manufacturing and design [14–16]. In addition to the already mentioned perfect hinges, the production of pantographic specimens at low scales, including the nano-scale, has been addressed [17–19].

Generally speaking, pantographic materials are based on the pantographic motif, *i.e.* a mechanism which is well known from everyday life (pantographic mirrors, expanding fences, scissor lifts, etc.), which is characterized by a zero-energy accordion-like homogeneous extension/compression deformation mode. For example, pantographic beams, strips of pantographic fabrics consisting of the periodic repetition in one direction of a single pantographic cell, have been proposed as an example of complete second gradient beam [20–23].

One of the main advantages of additive manufacturing lies in the possibility of easily producing complex three-dimensional geometries at, practically, no additional cost. For this reason, the development of 3D-printing techniques witnessed in the last two decades has stimulated research in the field of mechanical metamaterials. These materials assume special properties depending on their microstructure. Complex microstructures have been proven to confer remarkable macro-scale properties to metamaterials, like extension–bending/extension–torsion coupling [24–27], band gap properties for vibration attenuation [28–30], extreme stiffness [31], fluid-like behavior [32], extreme elastic range [33,34], damage-tolerant behavior [35], enhanced and/or tailored stability properties [36,37], unidirectional response [38,39], and many others [40]. In particular, it is very interesting the extension of the model and methodology presented in this work to the study of MEMS (Micro Electro-Mechanical Systems) or NEMS (Nano Electro-Mechanical Systems), following, *e.g.*, the suggestions on deformations of flexoelectric pantographic structures reported in [41].

The design of printed structures, which could be in principle done through topological optimization techniques [42] requires a thorough quantitative understanding of the mechanical behavior of the structure to be printed. Continuum models are needed to describe the large-scale mechanical behavior of a wide class of materials that, at some spatial scale, possess a microstructure. These models are particularly important for bridging spatial scales ranging from that of interactions between elements of the microstructure to the collective behavior of a large number of elements [43]. In the last ten years, making use of generalized and second gradient continua theories introduced in the early 1960s [44–46], many investigations were carried out dealing with pantographic structures. Indeed, thanks to their simple repeated pattern, pantographic structures can serve well as an exemplification of many issues in different fields of Solids Mechanics. Just to name a few, we can mention the homogenization of discrete systems resulting in second gradient continua [47], the identification of discrete [48] and semi-discrete models [49], the analysis and formulation of generalized shell theories [50,51], applications of functional analysis [52] like those making use of anisotropic Sobolev spaces [53,54], parameter optimization of discrete systems and gradient continua [55–57], numerical analysis of systems with higher regularity [58,59], and many others.

Discrete simulations can be designed that provide trajectories and distribution of strain energies at the element scale. Therefore, discrete models can be used as a more refined description than continuum models. While continuum models are less computationally demanding than discrete models, the formulation of continuum models able of capturing the behavior of a material with micro-structure, as well as the development of robust numerical procedures that work in sometimes-singular cases, is still challenging and, in any case, requires the utilization of discrete simulations for validation purposes. Therefore, when exploring the behavior of a material with micro-structure, while less appealing in view of getting analytical expressions, the utilization of discrete simulations is of utmost utility. In this paper, we exploit discrete modeling to numerically simulate the propagation of transverse impulses in pantographic beams. The large displacements regime is addressed by means of a simple yet efficient time-stepping scheme that allows to reconstruct the motion. Because of the intrinsic non-local properties of pantographic structures, which can be traced back to the existence of the above-mentioned zero-energy mode, displacement waves are extremely slow with respect to strain, *i.e.* extensional and bending, waves. For this reason, the features of strain waves, such as their variance and centroid, have been studied to characterize wave propagation in pantographic beams. Remarkable results were observed in terms of ergodicity and wave dispersion.

The work is organized as follows. Section 2 deals with the discrete modeling of pantographic beams via elastic springs. Section 3 illustrates briefly the time-step integration scheme used to solve the nonlinear equations of motion, while Section 4 presents the numerical simulations. Finally, conclusions and outlooks are briefly sketched.

2. Discrete modeling of pantographic beams *via* elastic springs

Let us consider the mechanical system depicted in Fig. 1 – known as pantographic beam or, in brief, as p-beam. Roughly speaking, the p-beam is obtained juxtaposing along the horizontal x-axis several cross-like unit cells. Each unit cell is made up of two beam-like elements connected through elastic pivots.

As mentioned in the introduction, several papers dealing with pantographic lattices formed by two families of orthogonal, [35,60–62], and non-orthogonal, [12], beams, and with pantographic beams [22,63] appear in the technical literature. Sometimes, the beam elements of the p-beam were modeled by semi-discrete approaches based on classical beam theories, as reported in [64–66]. The numerical results reported in the aforementioned references prove that the spring system sketched in Fig. 1 is able to describe effectively, and in a very simple manner, real prototypes realized, *e.g.*, by additive manufacturing.

This kind of description of the mechanical behavior of the p-beam is based on two types of interactions: *(i)* those modeled by extensional springs and *(ii)* those modeled by rotational springs. These two kind of interactions describe, in a

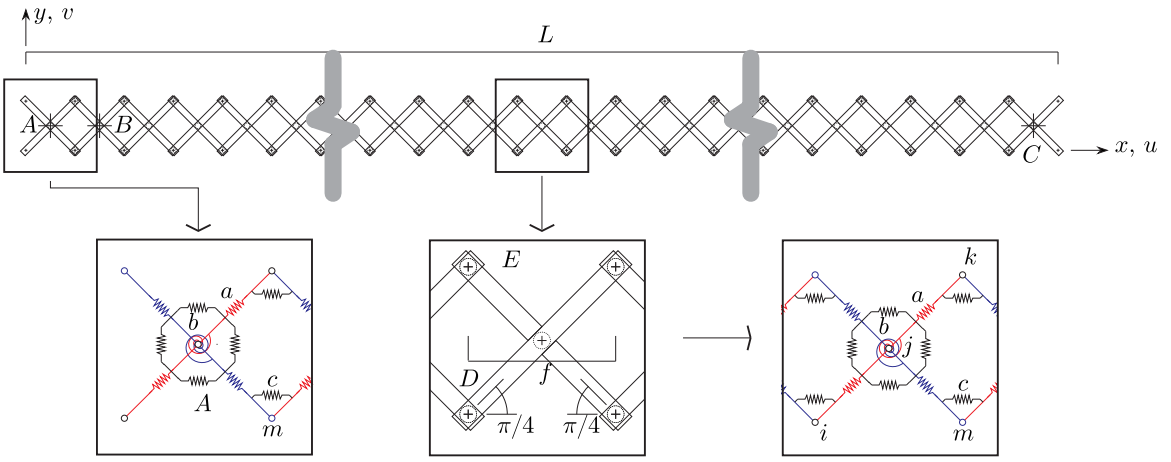

Fig. 1. Pantographic beam: geometry and discrete model.

very simple way, the reaction of the beams when they are stretched or bent. In addition, rotational springs are employed to describe the torsional stiffness of the pivot connecting different beam-like elements.

Clearly, this quite primitive description of the mechanical behavior of the pantographic beam could be enhanced following different routes. One route consists in modeling each slender element of the unit cell as a discrete Timoshenko beams, thus obtaining a more refined description, see, *e.g.*, [67]. Another route consists in using the so-called *h*-refinement strategy, see [48] for details. In such a strategy, each beam-like element is described by more than one extensional and rotational spring, in such a way that the discrete approximation of beam-like elements is improved. Obviously, the same strategy can be applied if the shear deformation of the beam-like elements cannot be neglected, *i.e.* regarding the beam-like elements as Timoshenko beams.

In the simplest case,[1] *i.e.* the beam-like elements are described by using the Euler–Bernoulli theory and no *h*-refinement strategy is used, the strain energy stored in each spring used to describe mechanical interactions is given by the following expressions:

$$\begin{aligned} E_a &= \frac{1}{2} a \Delta\ell^2 \,, \quad \text{beam stretching energy,} \\ E_b &= b(1+\cos\beta) \,, \quad \text{beam bending energy,} \\ E_c &= \frac{1}{2} c \left(\gamma - \frac{\pi}{2}\right)^2 \,, \quad \text{pivot torsional energy.} \end{aligned} \tag{1}$$

The springs in Fig. 1 are distinguished by means of three different colors: red and blue colors indicate extensional and bending (rotational) springs, black color indicates torsional (rotational) springs. Strain measures, $\Delta\ell$ for the stretching, $1+\cos\beta$ for the bending, and $\gamma - \pi/2$ for the torsion, can be computed by using only current positions of nodes of the p-beam or, equivalently, their nodal displacements.[2] In detail, the strain measures can be computed by means of the quantities

$$\begin{aligned} \Delta\ell &= \|p_j - p_i\| - \|P_j - P_i\| \,, \quad \text{stretching,} \\ \cos\beta &= \frac{\|p_j - p_i\|^2 + \|p_k - p_j\|^2 - \|p_k - p_i\|^2}{2\|p_j - p_i\|\|p_k - p_j\|} \,, \quad \text{bending,} \\ \gamma &= \arccos \frac{\|p_j - p_m\|^2 + \|p_k - p_j\|^2 - \|p_k - p_m\|^2}{2\|p_j - p_m\|\|p_k - p_j\|} \,, \quad \text{shearing,} \end{aligned} \tag{2}$$

where P_i and p_i are the reference and current positions of the *i*-, *j*-, *k*- and *m*th node, respectively, see Fig. 2 and also Fig. 1.

We remark that, since for the *i*th node $p_i = P_i + \mathbf{u}_i$, with $\mathbf{u}_i = (u_i, v_i)$ being its displacement, the stretching elementary contributions to the strain energy depend only on the displacements $\mathbf{u}_i$ and $\mathbf{u}_j$. Conversely, the bending contributions depend on $\mathbf{u}_i$, $\mathbf{u}_j$, and $\mathbf{u}_k$, while the torsional ones depend on $\mathbf{u}_j$, $\mathbf{u}_m$, and $\mathbf{u}_k$. In addition, we also remark that, see Eq. (2),

[1] The interested reader will find a more detailed discussion about this in [68].

[2] Pantographic beam nodes are depicted in Fig. 1 as small circles located at the intersection points between the beam-like elements.

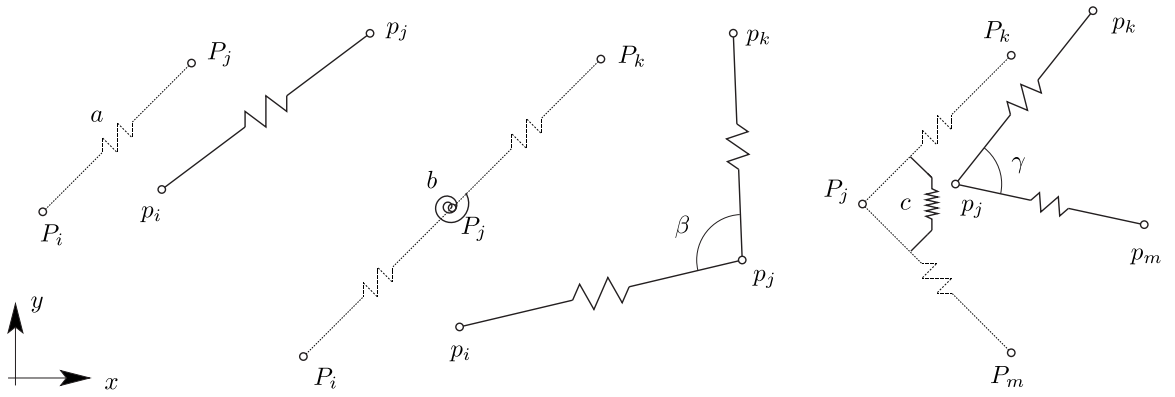

Fig. 2. Kinematics of stretching (left), bending (middle) and shearing (right) of the spring model (dashed and continuous lines indicate the reference and the current position, respectively).

stiffnesses used for specifying the mechanics of the pantographic beam are denoted a, b and c, for extensional, bending and torsional springs, respectively.[3]

We remark that the elementary strain energy contributions stored within each spring, and therefore the total strain energy of the p-beam, which govern its mechanical behavior, could take forms different from Eq. (2), see, *e.g.*, the elementary bending energy contributions E_b reported in [20,69].

After having introduced the elementary energy contributions above, finally, the p-beam strain energy E can be easily obtained by adding such contributions listed in (1). We choose as Lagrangian parameters of the system the nodal displacements collected within the vector $\mathbf{u}$. Then, we define the structural reaction $\mathbf{s}$, in short the reaction, as the gradient of the total strain energy with respect to the Lagrangian variables

$$\mathbf{s}(\mathbf{u}) = \frac{\mathrm{d}E}{\mathrm{d}\mathbf{u}} \,. \tag{3}$$

Furthermore, we define the so-called stiffness matrix $\mathbf{K}(\mathbf{u})$ as the Hessian of the strain energy or, equivalently, the gradient of the reaction $\mathbf{s}$

$$\mathbf{K}(\mathbf{u}) = \frac{\mathrm{d}\mathbf{s}}{\mathrm{d}\mathbf{u}} \,. \tag{4}$$

The gradient and the Hessian of the p-beam strain energy are the only tools necessary to construct a stepwise strategy able to solve the nonlinear equilibrium equations, when static problems are considered. Since in this work we want to deal with the dynamical behavior of p-beams, then we shall introduce the kinetic energy of the whole system. To this end, we include two kind of contributions. The first considers the mass distributed along the beams and the second the mass of pivots. In detail, by considering a one-dimensional link having length ℓ_e, the first contribution reads as

$$\frac{1}{2}\int_0^{\ell_e} \rho_e A_e \mathbf{v}(x)\cdot\mathbf{v}(x)\mathrm{d}x = \frac{1}{2}\dot{\mathbf{u}}_e \cdot \left(\int_0^{\ell_e} \rho_e A_e \mathbf{B}_e^T \mathbf{B}_e \mathrm{d}x\right)\dot{\mathbf{u}}_e = \frac{1}{2}\dot{\mathbf{u}}_e \cdot \mathbf{M}_e \dot{\mathbf{u}}_e \,, \tag{5}$$

where ρ_e, A_e and $\mathbf{v}$ are the mass density of the link, its cross-section area and its velocity vector, respectively. This last can be written in a form more suitable from the computational point of view by using the matrix of the shape functions $\mathbf{B}_e$ – we choose linear shape functions in this work – and the Lagrangian velocities collected in the vector $\dot{\mathbf{u}}_e$. The matrix $\mathbf{B}_e$, making use of the local coordinate $0 \leq \eta = x/\ell_e \leq 1$ and of the 2×2 identity matrix $\mathbf{I}_2$, as

$$\mathbf{B}_e = \begin{bmatrix} (1-\eta)\mathbf{I}_2 & \eta\mathbf{I}_2 \end{bmatrix} . \tag{6}$$

If we consider links with uniform cross-section, some straightforward calculations leads to the elementary mass matrix contribution

$$\mathbf{M}_e = \frac{1}{6}\rho_e A_e \ell_e \begin{bmatrix} 2\mathbf{I}_2 & \mathbf{I}_2 \\ \mathbf{I}_2 & 2\mathbf{I}_2 \end{bmatrix} . \tag{7}$$

[3] Within this work, we assigned the same stiffness parameters a and c to all the beam-like elements – *i.e.* uniform and balanced pantographic structures are considered – and, in addition, we assigned, for and within each unit cell, the same pivots' torsional stiffness c. Obviously, these hypotheses are not essential and can be easily removed to generalize the model.

Regarding the second contribution to the kinetic energy, the pth pivot mass matrix contribution can be written as

$$\mathbf{M}_p = \rho_p \frac{\pi d_p^2}{4} h \mathbf{I}_2 \,, \tag{8}$$

where d_p and h are the diameter and the height of the pth cylindrical pivot, respectively.[4]

The elementary mass matrix contributions reported in (7) and (8) are the only necessary quantities for assembling the mass matrix $\mathbf{M}$ by using a straightforward procedure similar to that required for the stiffness matrix. We remark that: *(i)* the mass matrix $\mathbf{M}$, in the considered case, can be recognized as a constant, *i.e.* it is not configuration-dependent; *(ii)* from the strain energy, the reaction $\mathbf{s}$ can be easily computed by means of (3). These are the only strictly necessary quantities to write down the system of ordinary differential equations of motion (Euler–Lagrange equations, see [71]) governing the dynamics of the pantographic beam. In matrix form, it reads

$$\mathbf{M}\ddot{\mathbf{u}}(t) + \mathbf{s}(\mathbf{u}(t)) - \mathbf{f}(t) = \mathbf{0} \,, \tag{9}$$

where, in addition to the Lagrangian parameters used for describing the motion – *i.e.* the displacement vector $\mathbf{u}$ and the acceleration vector $\ddot{\mathbf{u}}$ – the external force vector $\mathbf{f}$ appears.

3. Solving the nonlinear equations of motion through a time-step integration scheme

Selecting a reliable method to solve the system of nonlinear differential equations which governs the motion of a Lagrangian system is a delicate task. A quick look at technical references reveals that there are a lot of interesting contributions. In the Authors' opinion, a good starting point for scholars interested to this problem is Wriggers' book [72], which is updated until 2000. It discusses fundamental issues and examines some classic time step integration schemes such as those of Wilson and Newmark. More recent contributions are reported in the papers [73–75], which also contain several references.

Time-step integration schemes represent a very often pursued route for solving equations of motion. The key idea is the introduction of a time discretization, possibly non-uniform, suitable for the underlying problem. The goal of a stepwise integration scheme is recovering the equilibrium path – *i.e.* the pair made up of time, t, and the corresponding Lagrangian variables collected in the displacement $\mathbf{u}$ and velocity $\dot{\mathbf{u}}$ vectors – solving a series of initial value problems. In rough terms, for each time interval Δt – *i.e.* one of the intervals used to discretize the time – the solution at the end of the interval is computed starting from the solution at its beginning. It has to be remarked that the choice of an appropriate time length is crucial, in particular if nonlinear problems must be solved. A suitable choice for the time step length, especially if the underlying problem is complex, requires both some preliminary analyses and a noteworthy experience of the analyst.

For this reason, numerical integration schemes that cut preliminary analyses and reduce the analyst experience requirement should be, at least in principle, favored. In this regard, it is noteworthy the attempt of Casciaro [76]. The main appeal of his method consists in the adaptability to the (*a priori*) choice of the time step length. Unfortunately, although Casciaro's paper was published in an important journal such as *Meccanica* in 1975, his method is almost unknown to the majority of scientists which work in dynamics.

The key idea of Casciaro's method is the introduction of two free parameters that have to be to optimized to obtain the *best* dynamical response for the *a priori* chosen time step length. In detail, Casciaro started from the simple observation that the numerical solution of time evolution of a system is inevitably affected by errors depending on the chosen time step length Δt. These errors may be primed by time step lengths greater than a fraction of the minimum natural period of the considered system and, as a consequence, trigger numerical instabilities. Large time step lengths might also introduce spurious beatings, that is beating produced by numerical errors. Conversely, when the time step length is too small, round-off errors may be introduced biasing, even in a significant way, the quality of the numerical solution.

On the basis of the observations mentioned in the foregoing, Casciaro's scheme is founded on the following key points: *(i)* within a time interval, displacements time evolution is approximated by a quadratic interpolation law; the interpolation makes use of displacements and velocities at the beginning and at the end of the time interval[5]; *(ii)* the momentum–impulse relationship in discrete form.

The displacement vector $\mathbf{u}(t)$ within the time step $\Delta t = t_{k+1} - t_k$ can be written, changing its argument to the dimensionless variable τ, by using the quadratic rule

$$\mathbf{u}(\tau) = \mathbf{u}_k + (2\tau - \tau^2)\Delta t \left(\frac{1}{2} - \beta\right) \dot{\mathbf{u}}_k + \tau^2 \Delta t \left(\frac{1}{2} + \beta\right) \dot{\mathbf{u}}_{k+1} \,, \quad \tau = \frac{t - t_k}{t_{k+1} - t_k} \,, \tag{10}$$

where vectors $\mathbf{u}_k$, $\dot{\mathbf{u}}_k$ and $\dot{\mathbf{u}}_{k+1}$ collecting displacements and velocities at the beginning t_k of the time step and velocities at the end t_{k+1} of the time step, respectively, are used. This kind of interpolation has two remarkable properties: *(i)* it gives the quality of a quadratic interpolation law at a price similar to a constant law (on n time intervals only $n+2$ parameters

[4] We notice that this very simple hypothesis does not prevent to model p-beam with pivots having different torsional stiffness and kinetic energy. This can be useful for optimizing the pivots' diameter, see, *e.g.*, [70] for an interesting application.

[5] This law is analogous to that used by the B-spline interpolation, which, in turn, is the basis of modern NURBS. The same idea was used in 1985 by Aristodemo [77] to describe an efficient finite element for two-dimensional elastic problems.

are necessary, practically the same of a constant interpolation law); *(ii)* besides being a continuous law for displacements, this rule enforces also the continuity of velocities, thus producing a C_1 continuity in time.

The dimensionless coefficient β in Eq. (10) plays the role of weight between the two contributions of the velocities at the beginning $\dot{\mathbf{u}}_k$ and at the end $\dot{\mathbf{u}}_{k+1}$ of the time interval. It is enough to write the interpolation rule (10) at the end of the time step, *i.e.* for $\tau = 1$, for obtaining the equation

$$\mathbf{u}_{k+1} = \mathbf{u}_k + \Delta t \left(\frac{1}{2} - \beta\right) \dot{\mathbf{u}}_k + \Delta t \left(\frac{1}{2} + \beta\right) \dot{\mathbf{u}}_{k+1} \,. \tag{11}$$

Clearly, the dimensionless terms $\left(\frac{1}{2} - \beta\right)$ and $\left(\frac{1}{2} + \beta\right)$ that appear in (11) weight, along with the time step length Δt, the two velocity vectors at the beginning and at the end of the time step.

Besides the rule (11), Casciaro's numerical scheme also uses the momentum–impulse relationship in time-discrete form. In formulae it reads

$$\mathbf{M}(\dot{\mathbf{u}}_{k+1} - \dot{\mathbf{u}}_k) + \Delta t \left(\frac{1}{2} - \alpha\right) (\mathbf{s}_k - \mathbf{f}_k) + \Delta t \left(\frac{1}{2} + \alpha\right) (\mathbf{s}_{k+1} - \mathbf{f}_{k+1}) = \mathbf{0} \,, \tag{12}$$

where we distinguish two terms: *(i)* the momentum change, $\mathbf{M}(\dot{\mathbf{u}}_{k+1} - \dot{\mathbf{u}}_k)$; *(ii)* the average net impulse, this last is weighted by two dimensionless factors $\left(\frac{1}{2} - \alpha\right)$ and $\left(\frac{1}{2} + \alpha\right)$, which, as before, can be appropriately tuned selecting a suitable value for α. The two dimensionless parameters α and β, following Casciaro, can be tuned on the basis of: the time step length Δt and estimates of the first, T_1, and of the last, T_n, natural periods of the considered system. More specifically, an eigenvalue analysis involving the mass and stiffness matrices $\mathbf{M}$ and $\mathbf{K}$, this last evaluated in the reference configuration $\mathbf{K}(\mathbf{0})$, is preliminarily required.

In Casciaro's work [76], the law for choosing *optimally* the parameters α and β are provided. These formulae are based on the analysis of a one-degree-of-freedom system in linear regime. The aforementioned paper contained only a few details on the derivation of these laws, while a more extensive discussion is carried out in a series of reports published some years before. This fact, along with the fact that there were some typos in the formulae, most likely, caused that at the end Casciaro's idea was forgotten.[6]

The optimal values of the dimensionless parameters α and β are

$$\begin{aligned} \beta = -\alpha &= \sqrt{-\frac{1}{4} + \frac{1}{\delta^2} - \frac{1 + \sqrt{1 + \tan^2 \delta}}{2 \tan^2 \delta}} \,, \qquad 0 < \delta < \frac{\pi}{2} \,, \\ \beta = -\alpha &= \sqrt{-\frac{1}{4} + \frac{1}{\delta^2} - \frac{1 - \sqrt{1 + \tan^2 \delta}}{2 \tan^2 \delta}} \,, \qquad \frac{\pi}{2} < \delta < \pi \,, \end{aligned} \tag{13}$$

having introduced $\delta = 2\pi \Delta t / T_n$. We remark that Eq. (13), when $\Delta t \to 0$, leads to $\beta = -\alpha = 1/\sqrt{6}$. Instead, when $\Delta t \to T_n/2$, $\beta = -\alpha = 1/\pi$ is obtained.

Conversely, when $\Delta t > T_n/2$, the optimal values assume the form

$$\alpha = -\frac{T_n}{2\pi \Delta t} + \frac{c^3}{1 + 2c^3} \,, \quad \beta = \frac{T_n}{2\pi \Delta t} + \frac{c^3}{1 + 2c^3} \,, \quad c = \frac{2\Delta t - T_n}{T_1 - T_n} \,. \tag{14}$$

Formulae (14) contain both the sum of two terms: the first is a hyperbola branch which links the optimal values of α and β at the end of the interval $\Delta t < T_n/2$; the second is the ratio between two cubic polynomials, which tends – when $\Delta t \to \infty$ – to the value 1/2. Hence, the values of α and β corresponding to this case are able to reproduce a quasi-static solutions.[7]

At this point, before presenting the numerical results of the analysis, we sketch the solution strategy used to overcome the geometric nonlinearities of the p-beam reaction, *i.e.* to solve for each discrete time instant the nonlinear equilibrium equations. We start with the expansion of the reaction $\mathbf{s}_{k+1}$ by using a truncated Taylor series

$$\mathbf{s}_{k+1} = \mathbf{s}(\mathbf{u}_{k+1}, \dot{\mathbf{u}}_{k+1}) \approx \mathbf{s}_k + \mathbf{K}_k (\mathbf{u}_{k+1} - \mathbf{u}_k) \,, \tag{15}$$

where the stiffness matrix $\mathbf{K}_k$ computed at the beginning of the considered time interval is used. Using Eq. (4), we obtain

$$\mathbf{K}_k = \left.\frac{\mathrm{d}\mathbf{s}}{\mathrm{d}\mathbf{u}}\right|_{\mathbf{u}_k} \,. \tag{16}$$

[6] For the interested scholars, a more complete sketch of Casciaro's scheme along with correct formulae for optimal values of the parameters α and β is reported in [23].

[7] Obviously, when the problem is nonlinear small values of the time step length have to be used in any case.

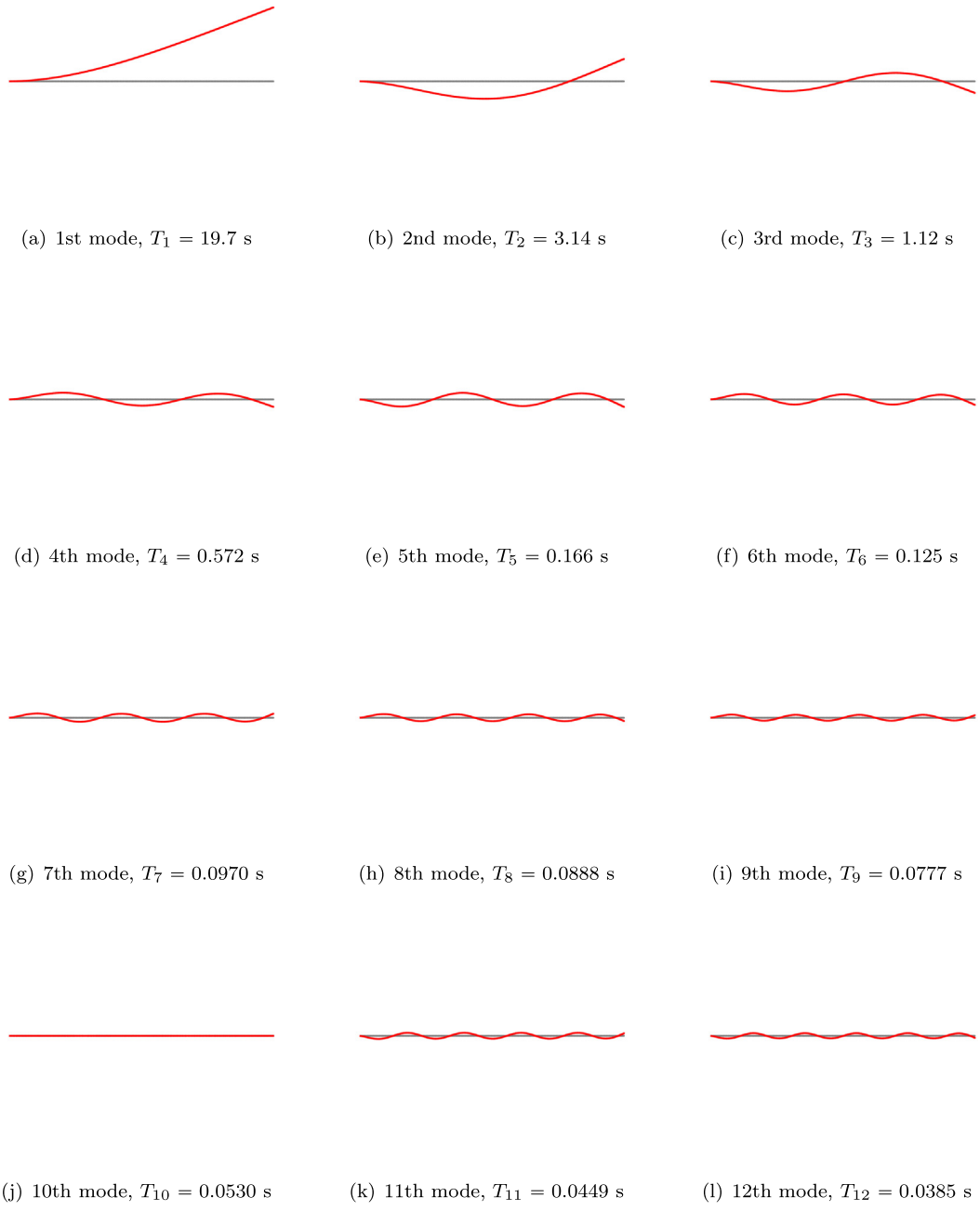

(a) 1st mode, $T_1 = 19.7$ s (b) 2nd mode, $T_2 = 3.14$ s (c) 3rd mode, $T_3 = 1.12$ s

(d) 4th mode, $T_4 = 0.572$ s (e) 5th mode, $T_5 = 0.166$ s (f) 6th mode, $T_6 = 0.125$ s

(g) 7th mode, $T_7 = 0.0970$ s (h) 8th mode, $T_8 = 0.0888$ s (i) 9th mode, $T_9 = 0.0777$ s

(j) 10th mode, $T_{10} = 0.0530$ s (k) 11th mode, $T_{11} = 0.0449$ s (l) 12th mode, $T_{12} = 0.0385$ s

Fig. 3. First twelve natural modes and periods of the p-beam. Red and gray colors denote the natural modes and the initial configuration, respectively. (For interpretation of the references to color in this figure legend, the reader is referred to the web version of this article.)

Remark that the displacement variables, *i.e.* $\mathbf{u}_{k+1}$, can be eliminated by using Eq. (11) from the system formed by Eqs. (11) and (12). Therefore, Eqs. (11)–(12), along with the definition of the stiffness matrix (16) and with the Taylor expansion (15), give the necessary tools to build a Newton-like algorithm for the considered problem. A good starting point is formula expressing the solution reminder calculated at the jth iteration

$$\mathbf{r}_j = \mathbf{M}(\dot{\mathbf{u}}_{k+1,j} - \dot{\mathbf{u}}_k) + \left(\frac{1}{2} - \alpha\right)(\mathbf{s}_k - \mathbf{f}_k) + \left(\frac{1}{2} + \alpha\right)(\mathbf{s}_{k+1,j} - \mathbf{f}_{k+1}), \tag{17}$$

a new estimate of the solution is found in a Newton-like way by the following recursive relation

$$\dot{\mathbf{u}}_{k+1,j+1} = \dot{\mathbf{u}}_{k+1,j} - \mathbf{H}_j^{-1}\mathbf{r}_j, \tag{18}$$

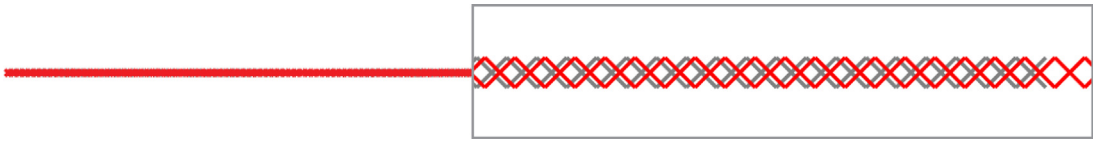

Fig. 4. Extensional mode (mode 10 in Fig. 3) for the considered p-beam. Red and gray colors denote the natural modes and the initial configuration, respectively. (For interpretation of the references to color in this figure legend, the reader is referred to the web version of this article.)

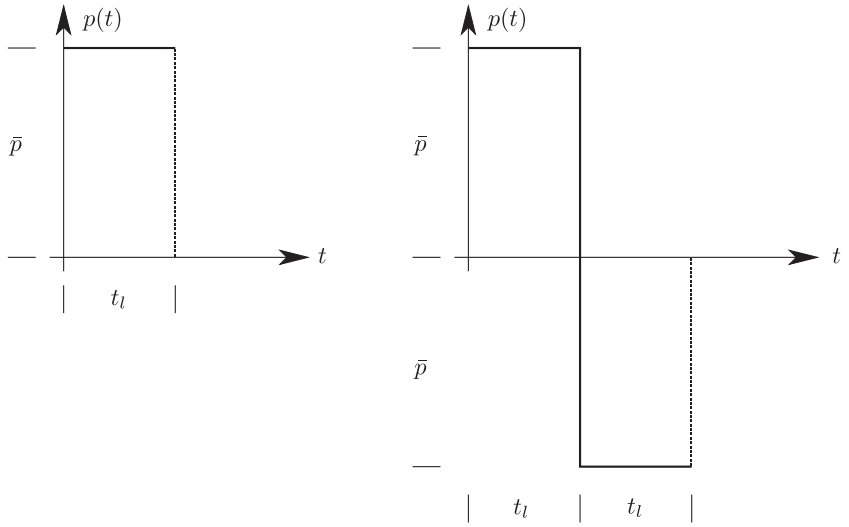

Fig. 5. Loading types: rectangular (on the left) and square wave (on the right) impulses.

where the iteration matrix $\mathbf{H}_j$ is defined as

$$\mathbf{H}_j = \nabla \mathbf{r}|_j = \mathbf{M} + \left(\frac{1}{2} + \alpha\right)\left(\frac{1}{2} + \beta\right)\mathbf{K}_{k,j}\,. \tag{19}$$

The matrix $\mathbf{K}_{k,j}$ in Eq. (19) is defined by Eq. (4) evaluated at the jth iteration of the Newton-like scheme performed within the current time step. It is worth remarking that Newton method is not able to get around limit points, *i.e.* configurations that make singular the iteration matrix. In the static case this is a formidable task since the iteration matrix coincides with the stiffness matrix but, in the dynamic case, the iteration matrix also includes the mass matrix, as it is evident from (19), which regularizes the problem, thus making usable the Newton scheme.

4. Numerical simulations

In this section we report on the results of numerical simulations carried out by making use of the modeling and solution procedures illustrated above. The scope of the analysis is to understand the propagation of waves in pantographic beams subjected to transverse impulses, *i.e.* time-dependent loads with compact support. To this end, as boundary conditions, to remove any kinematic indeterminacy, we choose to clamp the pantographic beams at its left end. More particularly, the position of the left end-node lying on the center line of the pantographic beam, *i.e.* node *A* in Fig. 1, is prescribed to remain fixed, while the central node of the adjacent cell, *i.e.* node *B* in Fig. 1, can move only horizontally, *i.e.* axially. The considered p-beam is constituted by 200 unit cells. The impulsive transverse load is applied to the right end-point of the pantographic beam lying on its center line, *i.e.*node *C* in Fig. 1. The geometrical parameters characterizing the considered p-beam are reported in Table 1 along with the material density and the spring stiffnesses, as required by the discrete model presented in Section 2. All the results given in the sequel must be considered to be expressed in the units of measure of the international system if not stated otherwise.

Using the numerical values reported in Table 1, we can compute the global mass and stiffnesses matrices of the system and, therefore, we can solve the eigenvalue problem giving the natural frequencies and modes. This analysis yields, in particular, the first T_1 and the last T_n natural periods of the p-beam which, along with the time step length Δt, completely determine the choice for the parameters α and β necessary to apply Casciaro's integration scheme, see Section 3.

Fig. 3 reports the first twelve natural modes computed in the reference configuration along with the corresponding natural periods. The first and the last natural periods of the discrete model of p-beam, for the chosen kinematic boundary

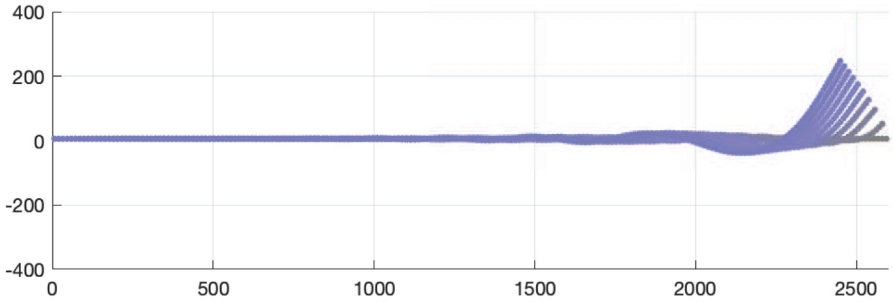

(a)

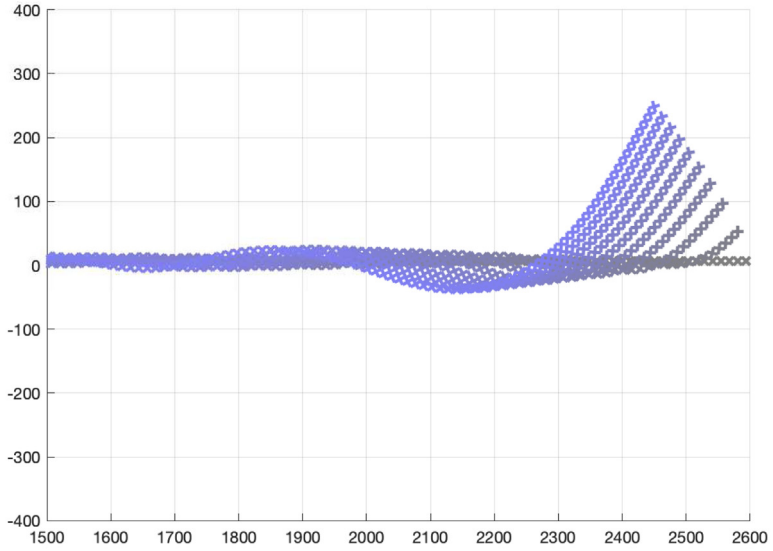

(b)

Fig. 6. Stroboscopic shoots of the p-beam (on the top) and their magnification in proximity of the free end (on the bottom).

Table 1
Dataset of geometrical and material parameters used in the present work.

cells	L	f	A	h	ρ	a	b	c
	mm	mm	mm^2	mm	kg/mm^3	N/mm	Nmm	Nmm
200	2600	13	1	2	930×10^{-9}	65000	20000	22000

conditions and the numerical values in Table 1, are $T_1 = 19.7$ s and $T_n = 3.3\times10^{-5}$ s, respectively. We remark that only the 10th mode is an extensional one among the first twelve modes (this is more clearly visible in Fig. 4 where a magnification is performed), which are all bending ones. Given that this mode is associated to the characteristic accordion-like behavior of pantographic structures, and as in the time evolution of nonlinear systems many modes interact with each other, this fact is particularly relevant. Indeed, as it will be clear in the sequel, the highly nonlinearity of the deformations studied in this paper is such that axial and transverse deformation caused by the transverse load are coupled to a non-negligible extent. Therefore, the characteristic behavior of pantographic beams in extension/compression has a relevant effect on the propagation of the perturbation caused by the external load in the transverse direction.

The impulse considered in the present study has rectangular and square wave shapes in time and is thus characterized by its amplitude $\bar{p}$ and its support, herein denoted with the symbol t_l, see Fig. 5. Zero initial nodal displacements and velocities are considered.

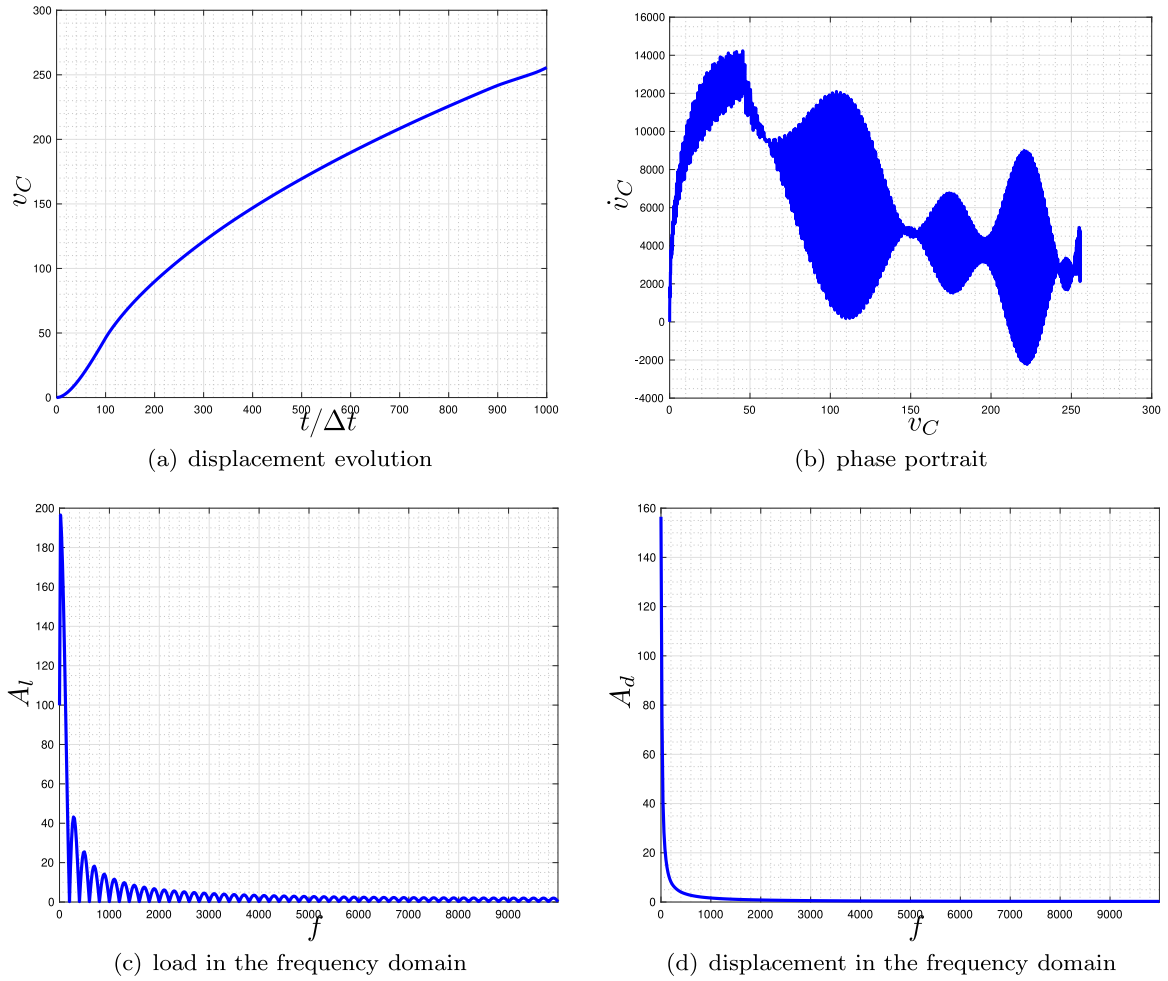

(a) displacement evolution

(b) phase portrait

(c) load in the frequency domain

(d) displacement in the frequency domain

Fig. 7. Evolution of the transverse displacement v_c of point C (a), phase portrait for the point C (transverse velocity *vs.* transverse displacement) (b). Magnitude of the discrete Fourier transform of the time-dependent external transverse load applied at point C (c) and of the evolution of the transverse displacement v_c of point C (d) as a function of the frequency.

According to the first and last natural periods, the time step length to be used for the time-integration scheme has been chosen equal to $\Delta t = 10^{-4}$ s. Obviously, the time horizon of the simulations t_v, *i.e.* the final time instant, has been chosen according to the phenomenon under consideration.

The first case study that we analyze is characterized by a rectangular load with $\bar{p} = 1000$ N and $t_l = 0.005$ s. Fig. 6 reports some stroboscopic shoots of the p-beam vibrations along with their magnification in proximity of the right end. It can be immediately observed that the deformation and the displacement induced by the transverse impulse force are extremely large. Indeed, looking at the stroboscopic pictures, the maximum transverse displacement reached within the beam, at its tip, is approximately 1/10th of the beam length. We also notice that the nodal displacement are decaying rather rapidly from the loaded tip to the left end of the pantographic beam.

Fig. 7 reports the evolution of the transversal displacement v_c of point C, the phase portrait for the point C (transverse velocity *vs.* transverse displacement) (b), the magnitude of the discrete Fourier transform of the time-dependent external transverse load applied at point C (c) and of the evolution of the transverse displacement v_c of point C (d) as a function of the frequency. It can be readily seen that the oscillation of the point C in the transverse direction has a period which is much larger than the time-support of the impulse. Such a period is indeed closer to the first natural period of the system. As the transverse displacement of the point C increases only in time in the considered time interval, the phase portrait does not show the presence of any cycle. From the phase portrait it can be concluded that the transverse velocity presents spurious numerical oscillations about a mean value that, however, do not affect the transverse displacement. It is questionable whether these oscillations are due to the chosen time-interpolation law for the displacement which produces a kind of Gibbs–Wilbraham phenomenon, see [78]. This issue will be the subject of future investigations.

As mentioned before, transverse nodal displacements decay rapidly from the right to the left end of the pantographic beam. This is partly due to the boundary conditions, which enforce a vanishing transverse nodal displacement at the

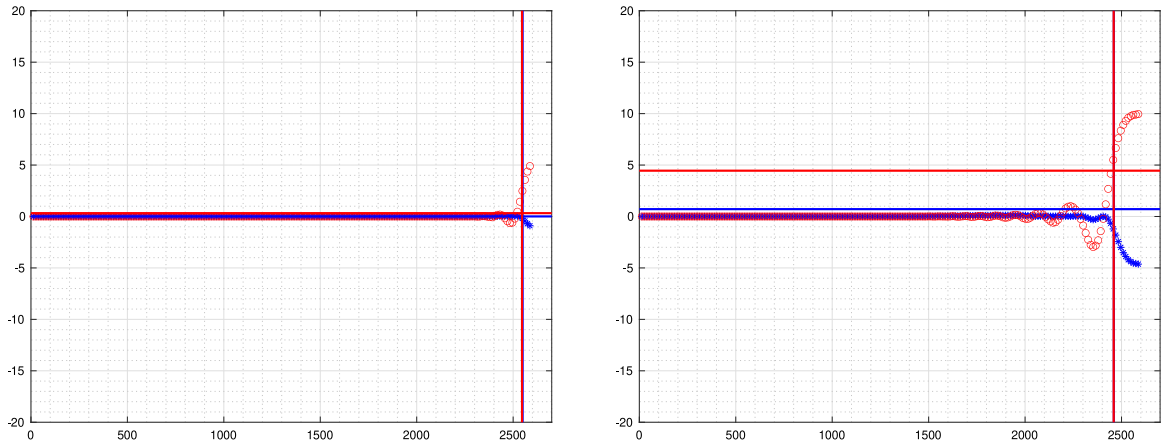

(a) $t/\Delta t = 50$ (b) $t/\Delta t = 200$

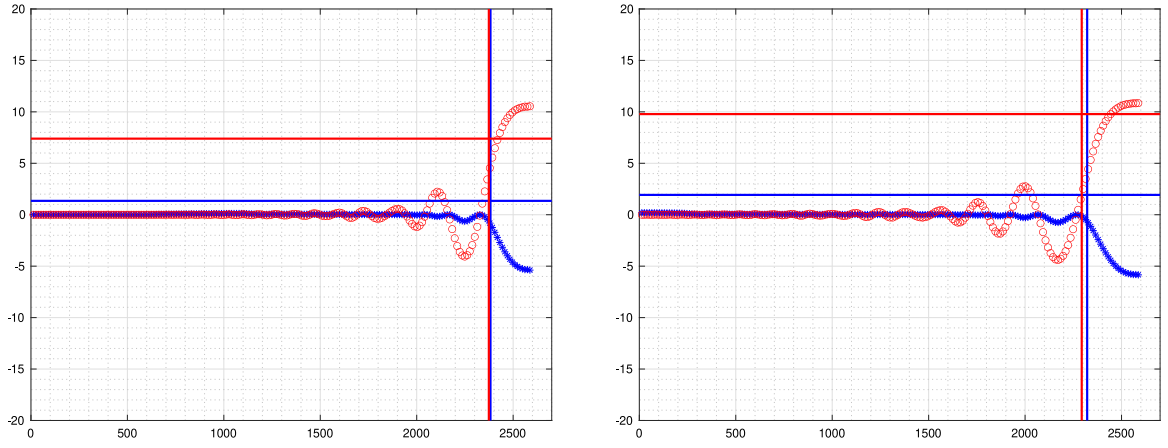

(c) $t/\Delta t = 350$ (d) $t/\Delta t = 500$

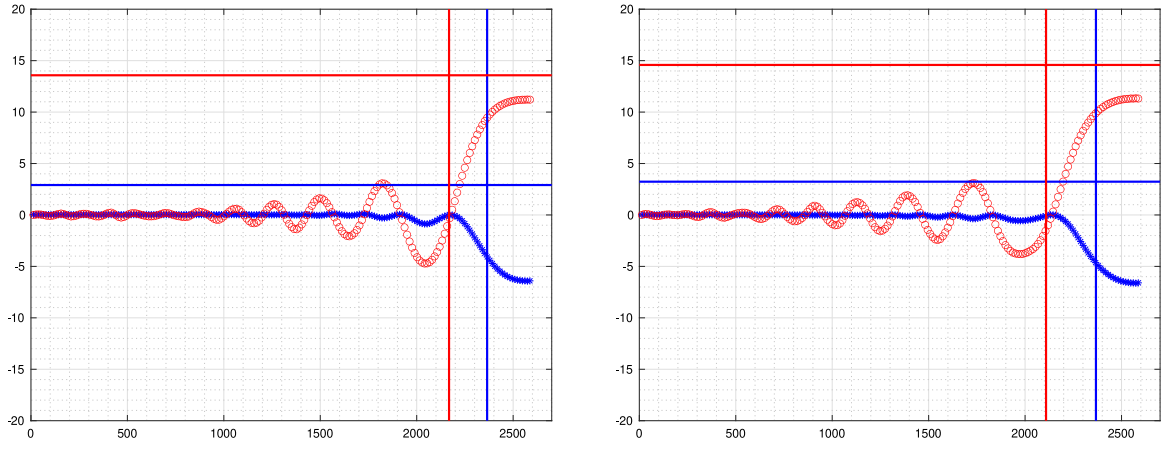

(e) $t/\Delta t = 800$ (f) $t/\Delta t = 950$

Fig. 8. Stroboscopic shoots illustrating the propagation of ε- and φ-waves for $t/\Delta t = 50$, 200, 350, 500, 800 and 950 for the case of the rectangular impulse with $\bar{p} = 1000$ N and $t_l = 0.005$ s. The vertical and horizontal lines indicate, respectively, the centroid and the variance of the same-color wave at a given time instant. Blue and red colors are associated, respectively, with $\varepsilon-$ and $\varphi-$waves. (For interpretation of the references to color in this figure legend, the reader is referred to the web version of this article.)

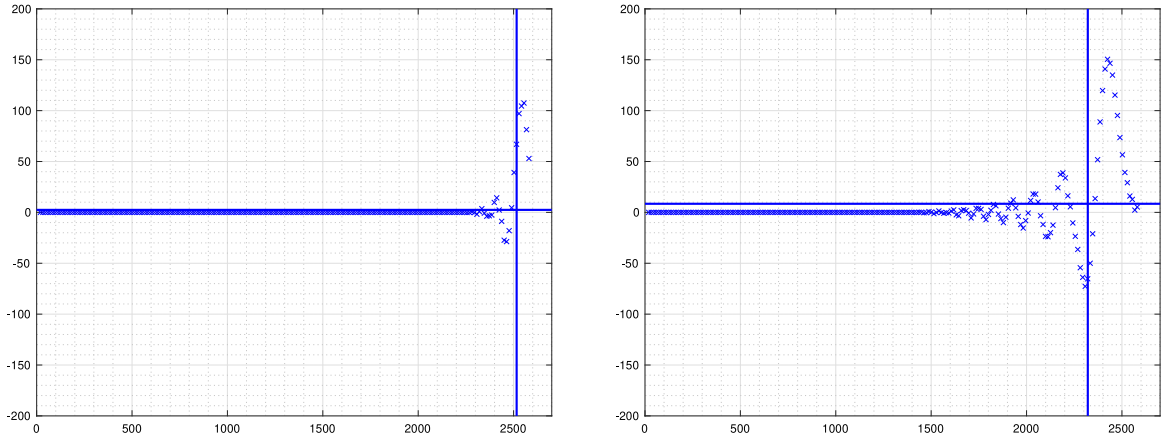

(a) $t/\Delta t = 50$ (b) $t/\Delta t = 200$

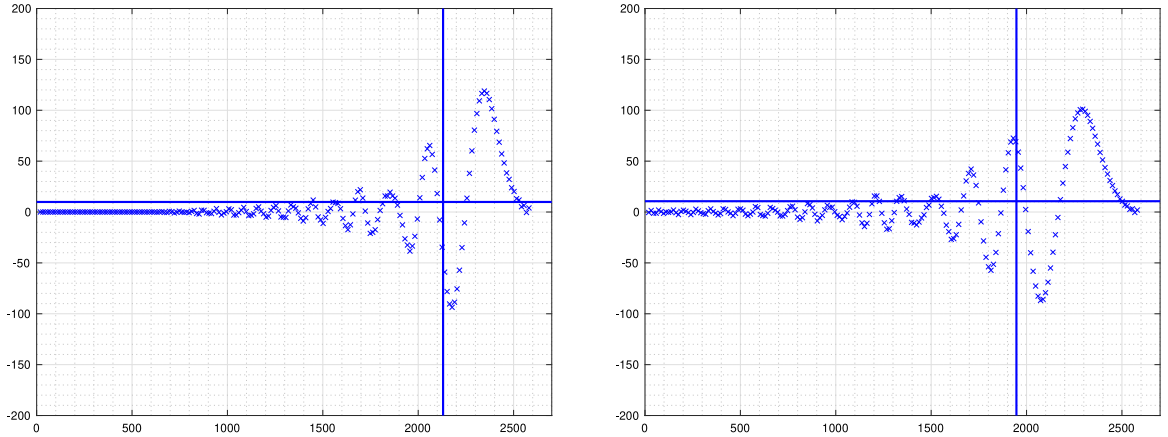

(c) $t/\Delta t = 350$ (d) $t/\Delta t = 500$

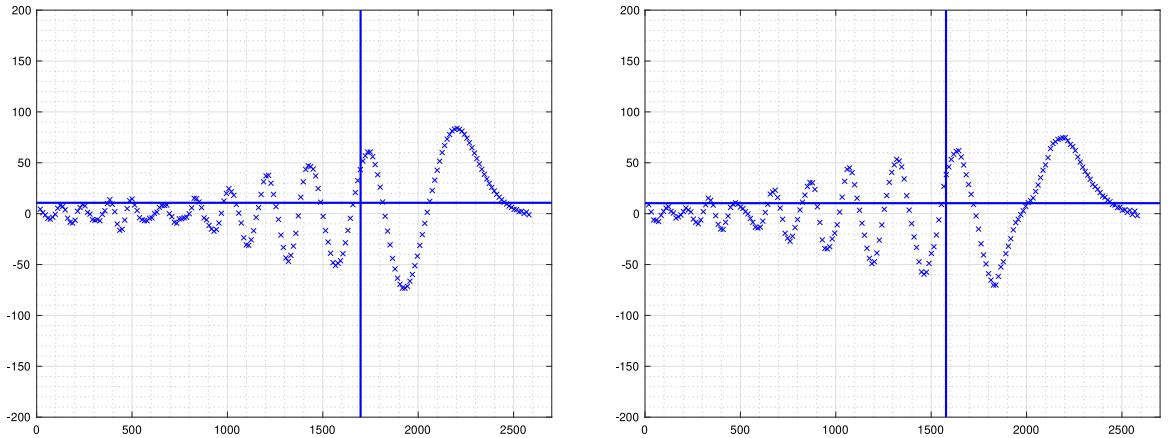

(e) $t/\Delta t = 800$ (f) $t/\Delta t = 950$

Fig. 9. Stroboscopic shoots illustrating the propagation of κ-waves for $t/\Delta t = 50$, 200, 350, 500, 800 and 950 for the case of the rectangular impulse with $\bar{p} = 1000$ N and $t_l = 0.005$ s. The vertical and horizontal lines indicate, respectively, the centroid and the variance of the wave at a given time instant.

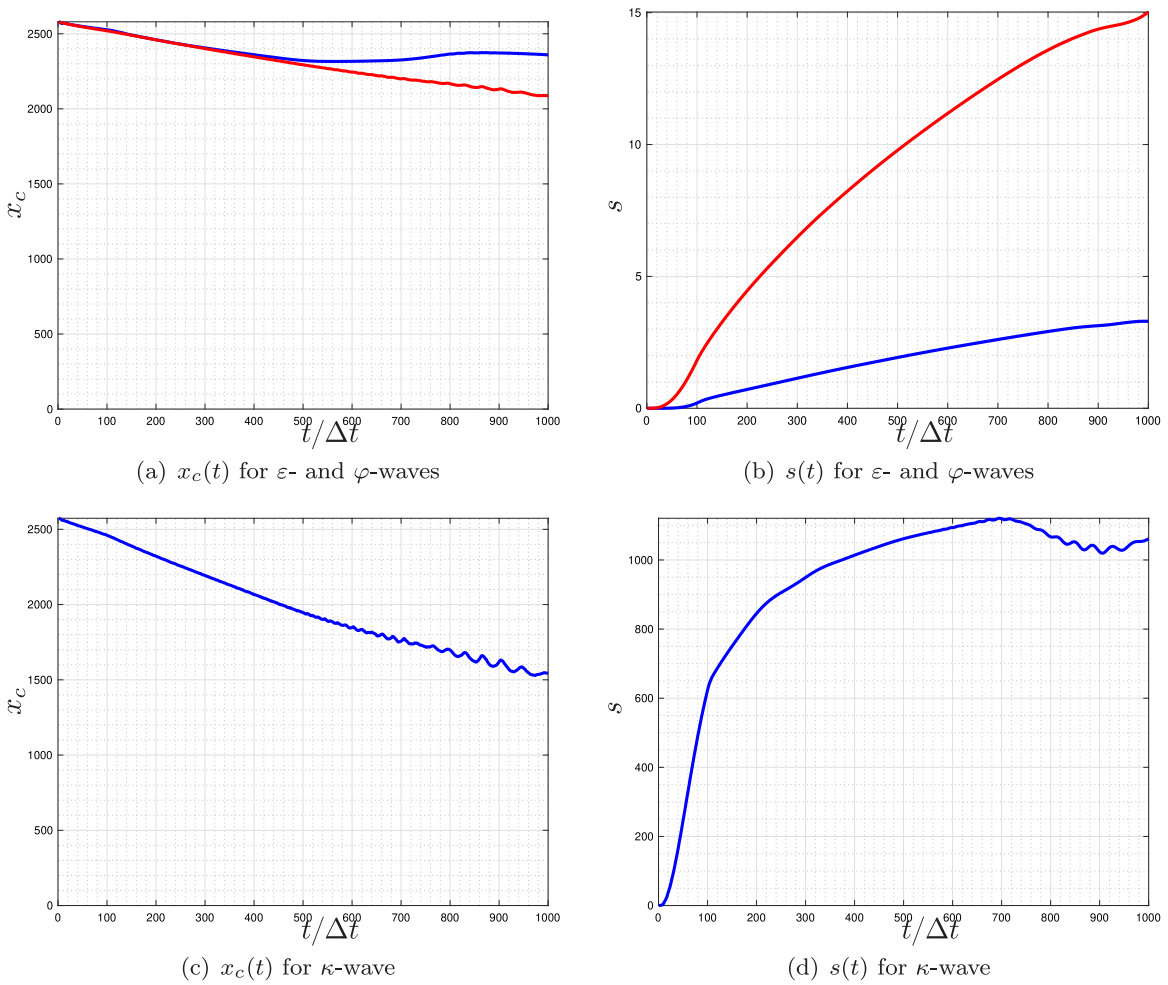

(a) $x_c(t)$ for ε- and φ-waves

(b) $s(t)$ for ε- and φ-waves

(c) $x_c(t)$ for κ-wave

(d) $s(t)$ for κ-wave

Fig. 10. Evolution of the centroid x_c and of the variance s for ε-, φ- and κ-waves in the case of the rectangular impulse with $\bar{p} = 1000$ N and $t_l = 0.005$ s. In the plots (a) and (b), blue and red colors refer to ε-, φ-waves, respectively. (For interpretation of the references to color in this figure legend, the reader is referred to the web version of this article.)

left end of the beam, and partly due to the fact that the beam is extremely compliant due to the accordion-like mode. For these reasons, it turns out that a convenient way of visualizing traveling waves along the pantographic beam is to look at strains instead of nodal displacements. Among the many possible strains that one could analyze, because of the slenderness of the structure and since we are interested with the present meso-scale study in guiding and validating the homogenization and understanding of the dynamic features of the pantographic beam, we concentrate ourselves on the classical strains of the (discrete) center line. Indeed, the first strain measure that we consider is its (discrete) elongation

$$\varepsilon = \frac{u_{i+1} - u_i}{\ell}, \quad \text{elongation,} \tag{20}$$

i.e. the difference of the horizontal displacement u of two consecutive pivots (i and $i+1$) of the p-beam divided by their distance ℓ in the reference configuration. We now define the linearized rotation angle of the segment connecting two adjacent nodes along the center line as

$$\varphi = \frac{v_{i+1} - v_i}{\ell}, \quad \text{unit length relative rotation,} \tag{21}$$

i.e. the difference of the vertical displacement v of two consecutive pivots (i and $i+1$) of the p-beam divided by their distance ℓ in the reference configuration. Having introduced this quantity, we are ready to define the second strain measure that we look at, namely the linearized (discrete) curvature of the center line

$$\kappa = \frac{v_{i+1} - 2v_i + v_{i-1}}{\ell^2}, \quad \text{bending,} \tag{22}$$

i.e. the finite difference approximation of the second derivative of the transverse displacement v.

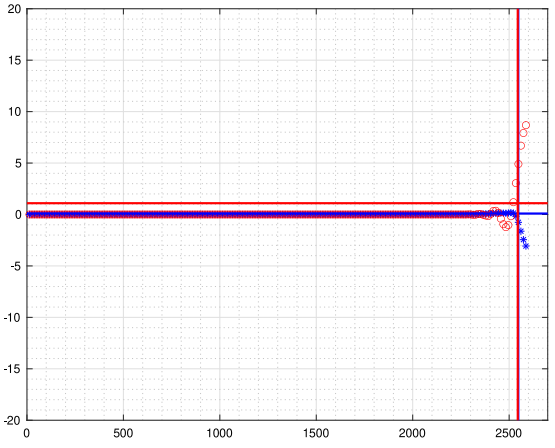

(a) $t/\Delta t = 50$

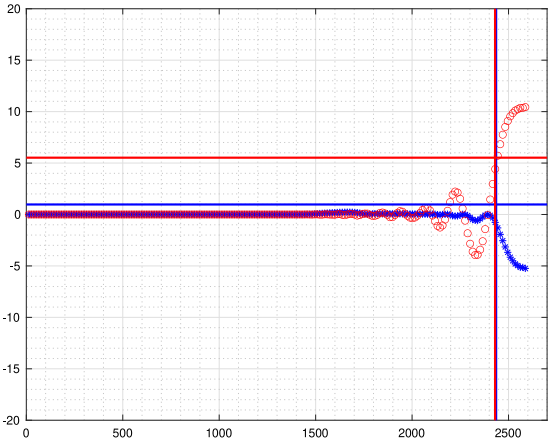

(b) $t/\Delta t = 200$

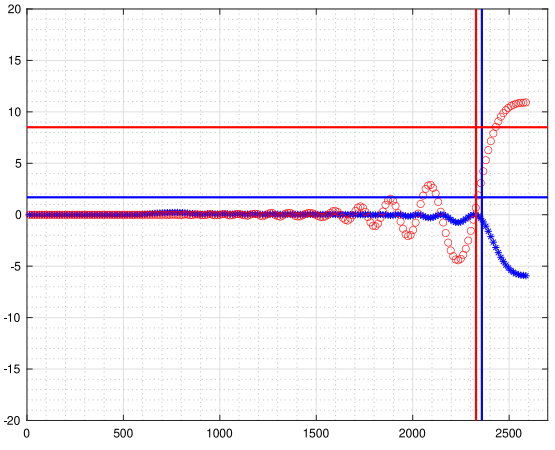

(c) $t/\Delta t = 350$

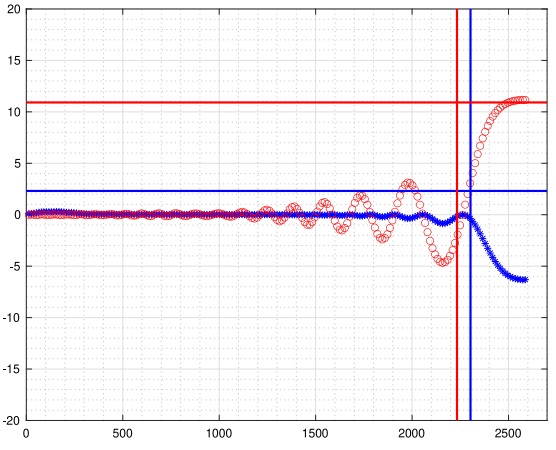

(d) $t/\Delta t = 500$

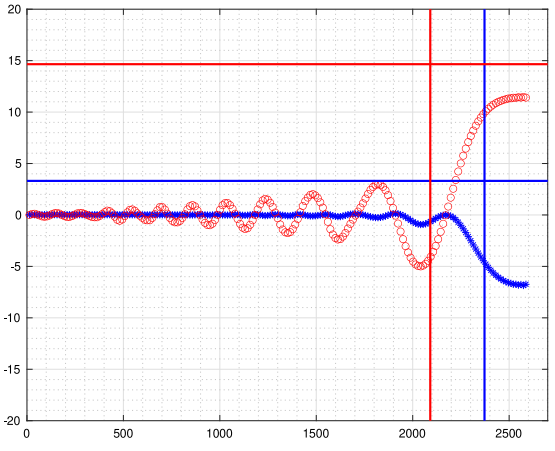

(e) $t/\Delta t = 800$

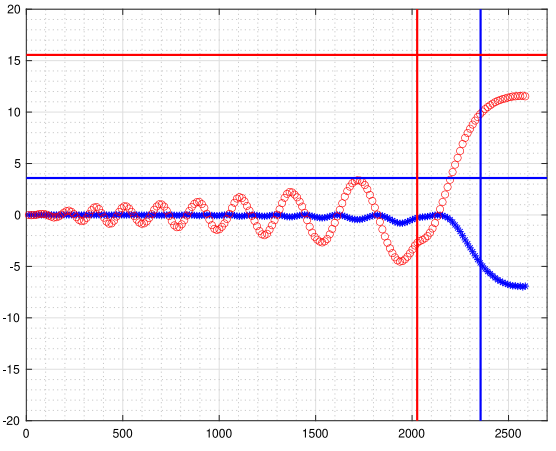

(f) $t/\Delta t = 950$

Fig. 11. Stroboscopic shoots illustrating the propagation of ε- and φ-waves for $t/\Delta t = 50$, 200, 350, 500, 800 and 950 for the case of the rectangular impulse with $\bar{p} = 2000$ N and $t_l = 0.0025$ s. The vertical and horizontal lines indicate, respectively, the centroid and the variance of the same-color wave at a given time instant. Blue and red colors are associated, respectively, with ε- and φ-waves. (For interpretation of the references to color in this figure legend, the reader is referred to the web version of this article.)

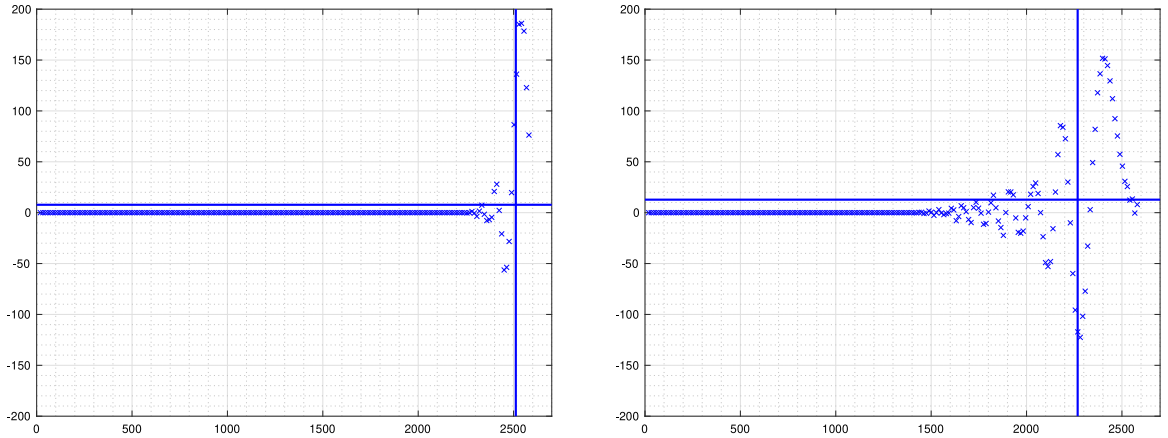

(a) $t/\Delta t = 50$ (b) $t/\Delta t = 200$

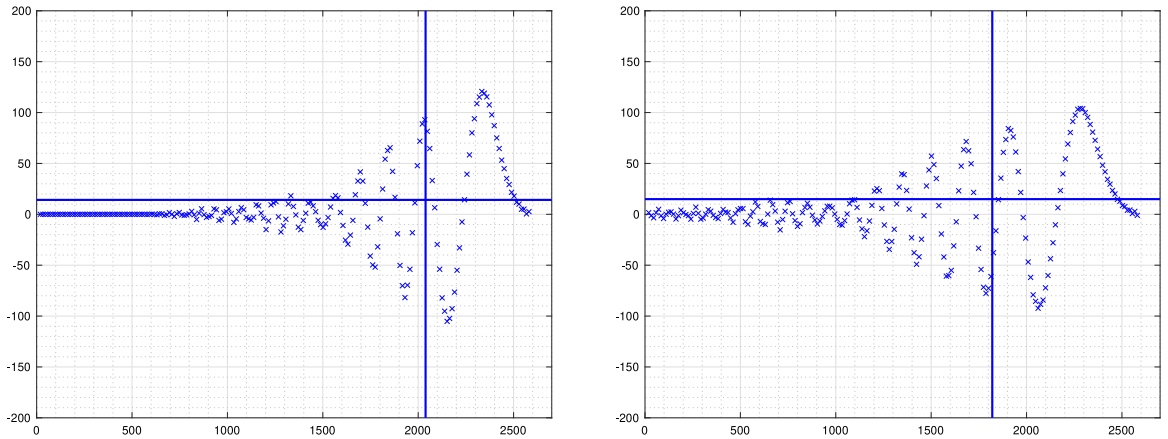

(c) $t/\Delta t = 350$ (d) $t/\Delta t = 500$

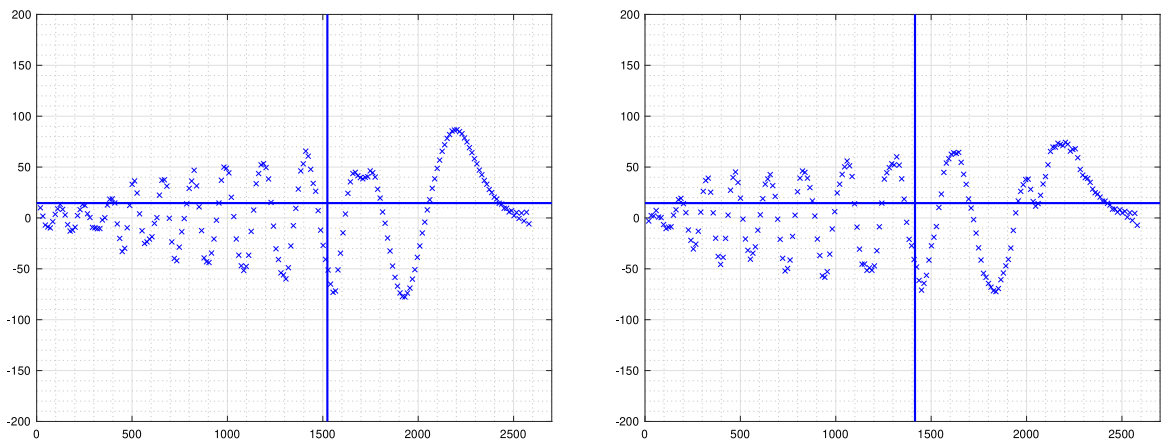

(e) $t/\Delta t = 800$ (f) $t/\Delta t = 950$

Fig. 12. Stroboscopic shoots illustrating the propagation of κ-waves for $t/\Delta t = 50$, 200, 350, 500, 800 and 950 for the case of the rectangular impulse with $\bar{p} = 2000$ N and $t_l = 0.0025$ s. The vertical and horizontal lines indicate, respectively, the centroid and the variance of the wave at a given time instant.

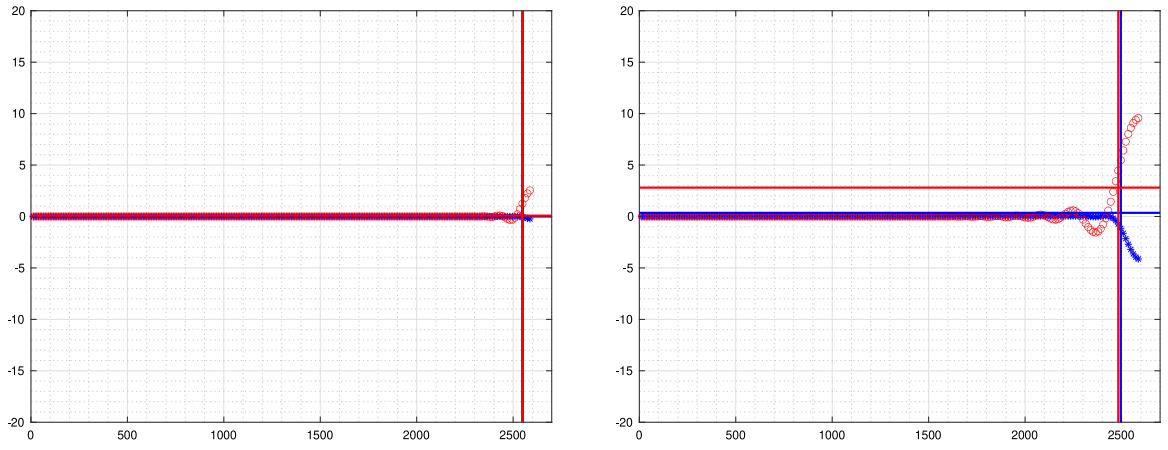

(a) $t/\Delta t = 50$ (b) $t/\Delta t = 200$

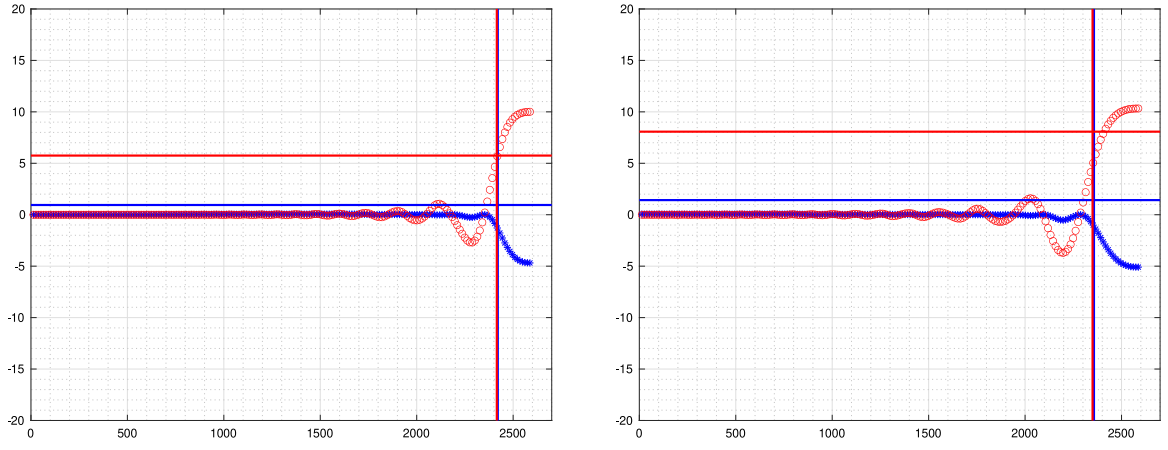

(c) $t/\Delta t = 350$ (d) $t/\Delta t = 500$

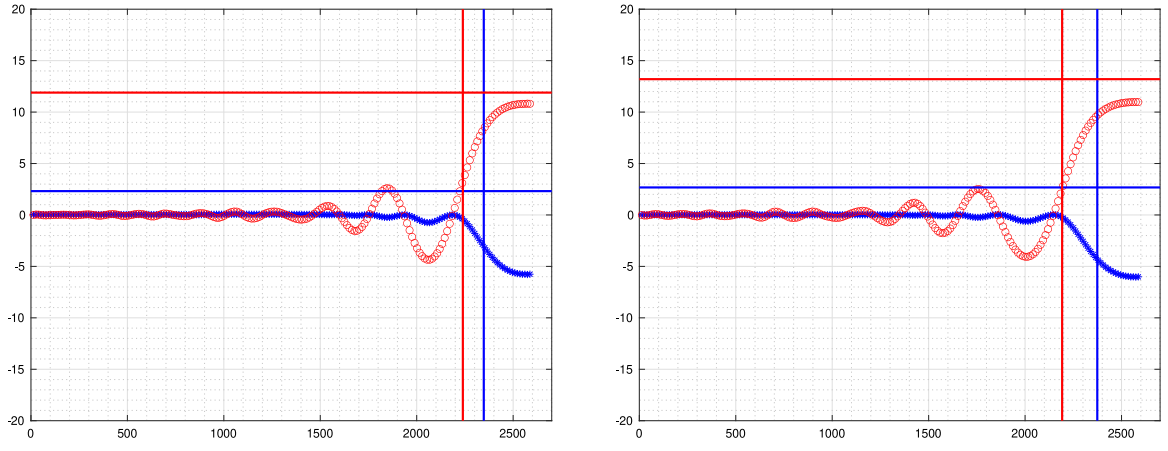

(e) $t/\Delta t = 800$ (f) $t/\Delta t = 950$

Fig. 13. Stroboscopic shoots illustrating the propagation of ε- and φ-waves for $t/\Delta t = 50$, 200, 350, 500, 800 and 950 for the case of the rectangular impulse with $\bar{p} = 500$ N and $t_l = 0.01$ s. The vertical and horizontal lines indicate, respectively, the centroid and the variance of the same-color wave at a given time instant. Blue and red colors are associated, respectively, with ε- and $\varphi-$waves. (For interpretation of the references to color in this figure legend, the reader is referred to the web version of this article.)

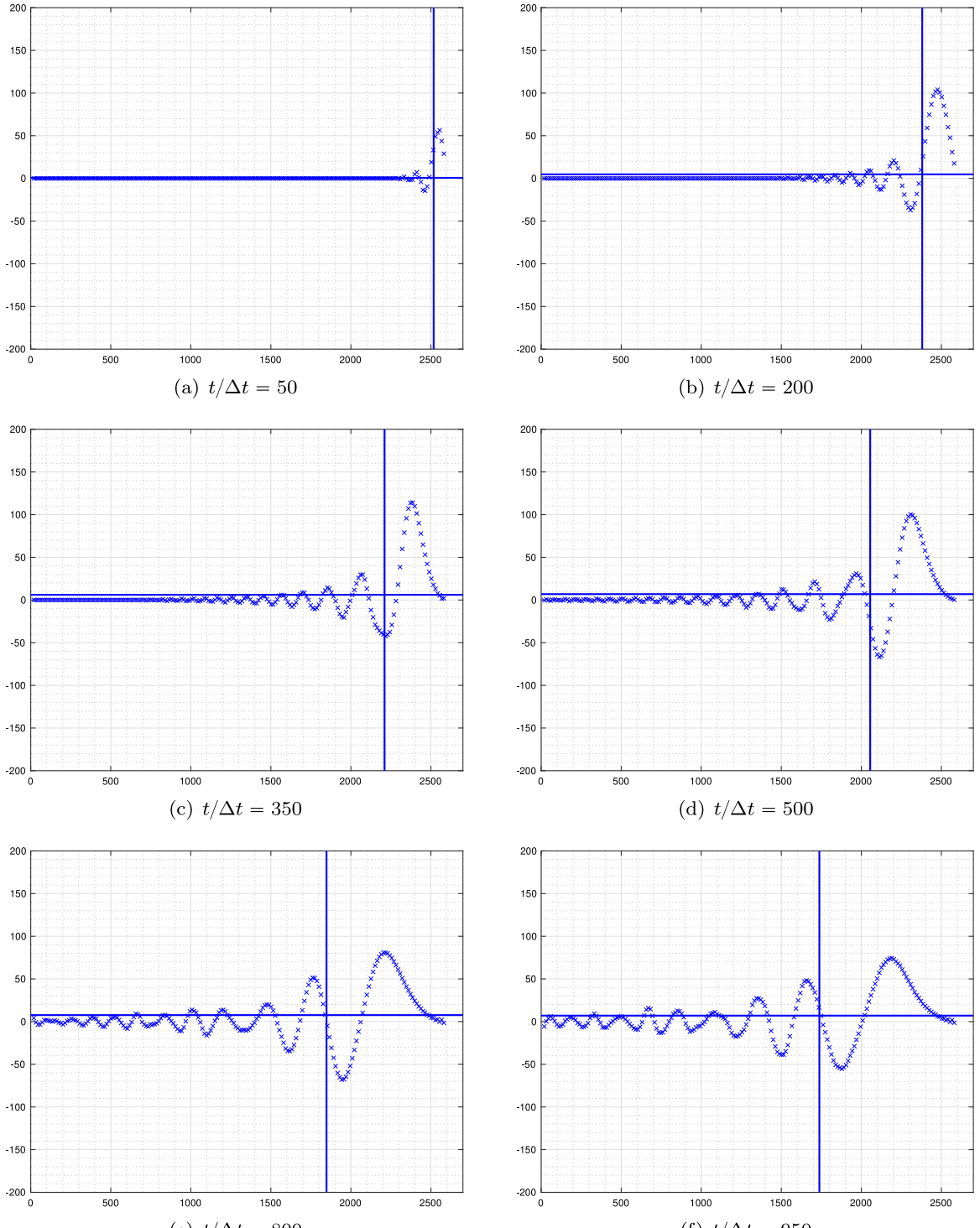

Fig. 14. Stroboscopic shoots illustrating the propagation of κ-waves for $t/\Delta t = 50$, 200, 350, 500, 800 and 950 for the case of the rectangular impulse with $\bar{p} = 500$ N and $t_l = 0.01$ s. The vertical and horizontal lines indicate, respectively, the centroid and the variance of the wave at a given time instant.

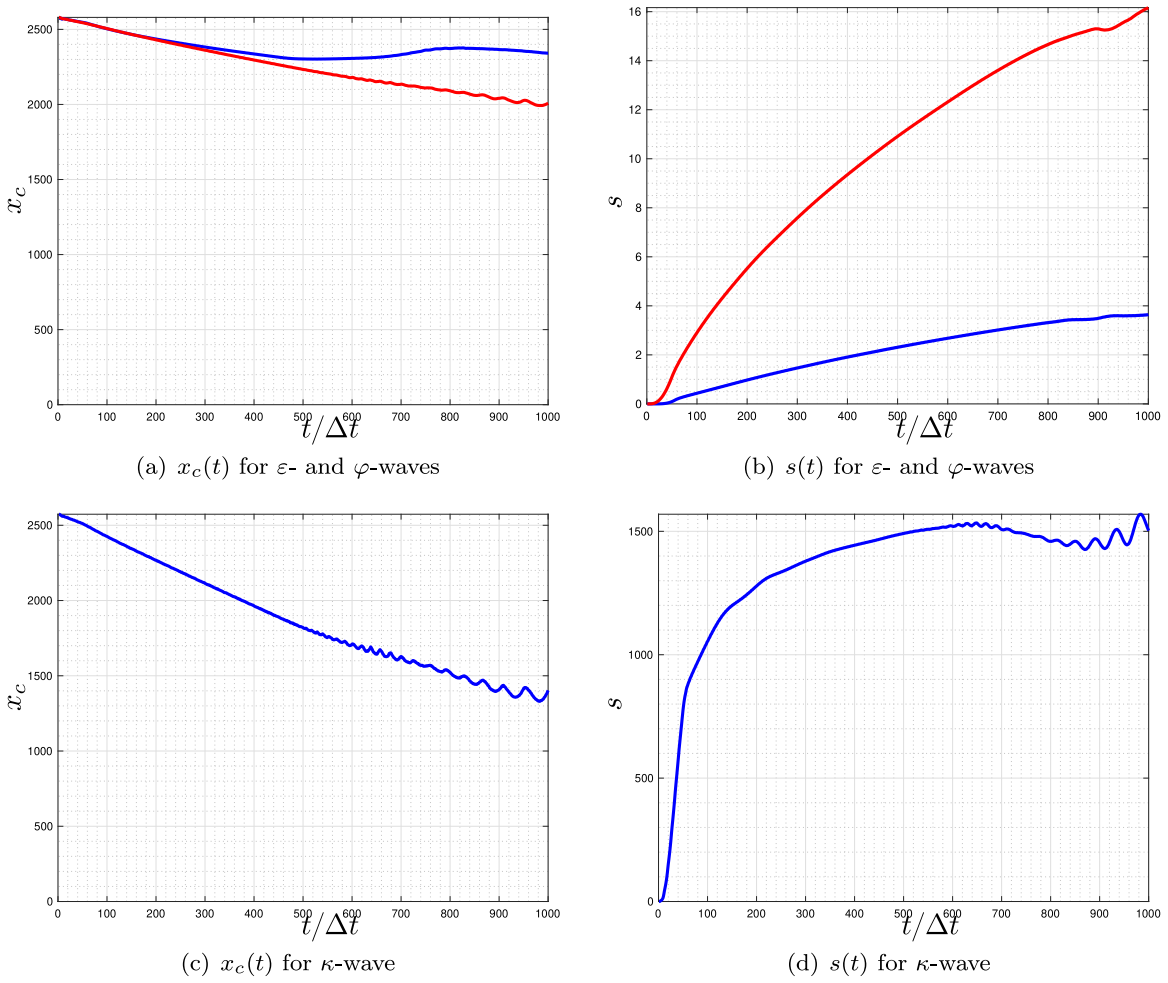

(a) $x_c(t)$ for ε- and φ-waves

(b) $s(t)$ for ε- and φ-waves

(c) $x_c(t)$ for κ-wave

(d) $s(t)$ for κ-wave

Fig. 15. Evolution of the centroid x_c and of the variance s for ε-, φ- and κ-waves in the case of the rectangular impulse with $\bar{p} = 2000$ N and $t_l = 0.0025$ s. In the plots (a) and (b), blue and red colors refer to ε- and φ-waves, respectively. (For interpretation of the references to color in this figure legend, the reader is referred to the web version of this article.)

In the subsequent figures we report, along with the plots of the propagating strain waves, showing the discrete strains of the center line defined above versus the unit cell number at a given time instant, two quantities which characterize to a large extent these waves, especially in view of measuring the change in shape of the propagating wave and its movement. Specifically, in the plots of the propagating strain waves, vertical lines indicate the position of the centroid x_c, along the reference axis of the beam, of the strain waves. Horizontal lines indicate the variance s of the strain waves. In formulae, the centroid position of a generic strain f is defined by

$$x_c = \frac{\sum_{i=1}^{n} |f_i| x_i}{\sum_{i=1}^{n} |f_i|}\,, \tag{23}$$

and its variance by

$$s = \frac{1}{n-1} \sum_{i=1}^{n} (f_i - \bar{f})^2\,, \tag{24}$$

where n is the number of nodes on which the function f is defined and $\bar{f}$ its mean value. Figs. 8 and 9 report, respectively, some stroboscopic shoots of ε, φ and κ as functions of the x-coordinate of the cell center, which illustrate their propagation. It can be noted that, at each time instant, the quantities ε and φ oscillate with the same velocity in space, while the quantity κ oscillates much more rapidly in space.

The evolution of the quantities x_c and s is worth to be studied because it provides an estimate of the wave velocity and of its dispersion. The strong advantage in dealing with these quantities is that their definition is purely kinematic and,

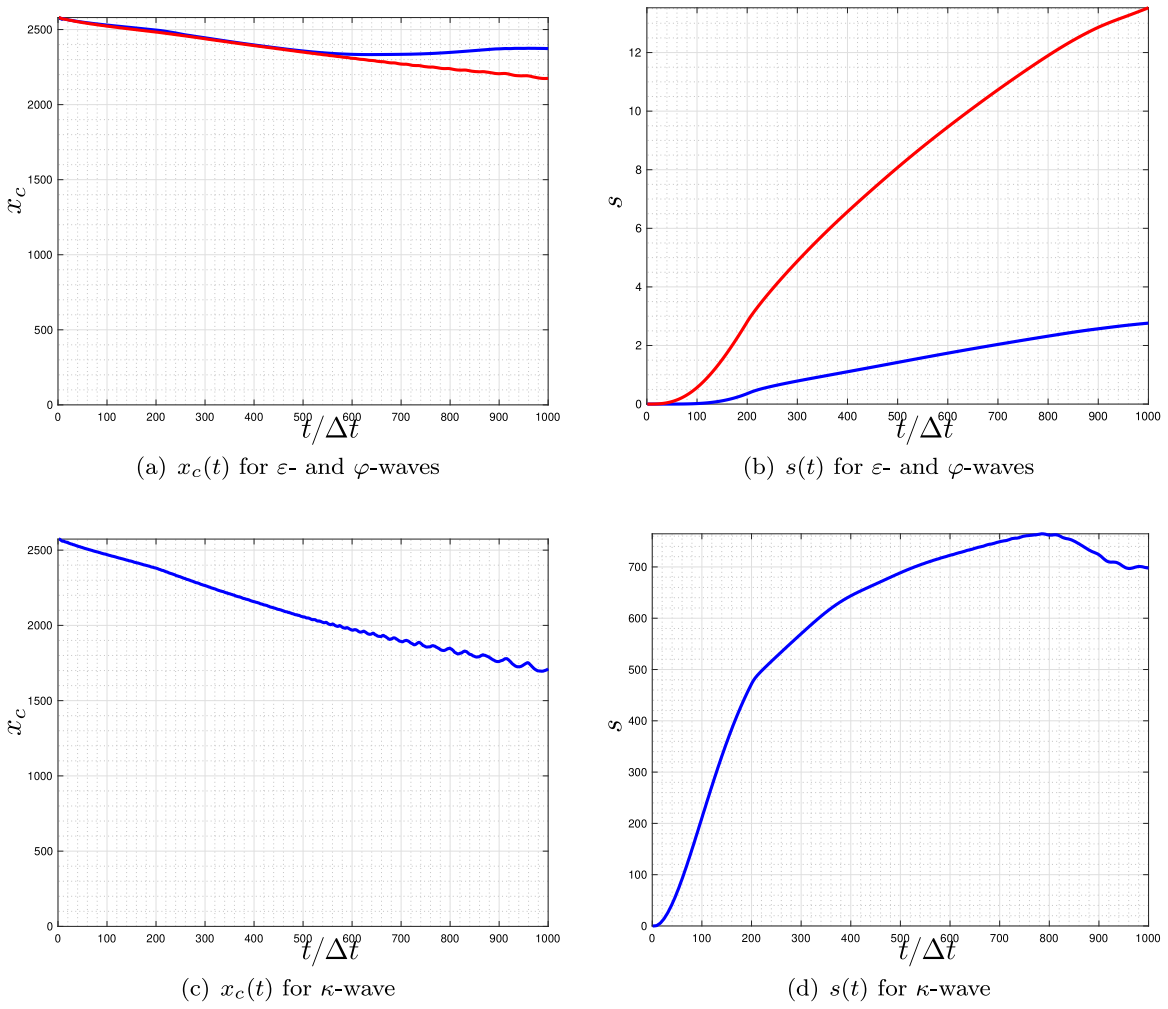

(a) $x_c(t)$ for ε- and φ-waves

(b) $s(t)$ for ε- and φ-waves

(c) $x_c(t)$ for κ-wave

(d) $s(t)$ for κ-wave

Fig. 16. Evolution of the centroid x_c and of the variance s for ε-, φ- and κ-waves in the case of the rectangular impulse with $\bar{p} = 500$ N and $t_l = 0.01$ s. In the plots (a) and (b), blue and red colors refer to ε- and φ-waves, respectively. (For interpretation of the references to color in this figure legend, the reader is referred to the web version of this article.)

therefore, they can be defined for any wave. The evolution of these quantities is reported for the case of the rectangular impulse with $\bar{p} = 1000$ N and $t_l = 0.005$ in Fig. 10. From this figure it can be concluded that the centroid position, for all the strain waves, advances with constant velocity in time until the wave interacts with the left boundary. This is a remarkable property as it allows to define clearly a wave velocity. After touching the boundary the strain waves are reflected and start interacting with incoming waves. This is indicated by the fact that their variance increases with reduced velocity until a stationary state is reached following composition of reflected and incoming waves giving, ideally, a constant variance in time and, practically, a variance oscillating around a given value. As the κ-wave travels which higher velocity than the ε- and φ-waves, this phenomenon is much more clearly visible in Fig. 10(d).

Aimed at studying the effect of the time-support of the impulse, we have considered for the rectangular impulse different values for the parameter t_l (see again Fig. 5). In particular, we have halved and doubled the value of the parameter t_l by keeping the area of the rectangle, *i.e.* the momentum entered into the system by the external world, unchanged.

Propagation of ε-, φ- and κ-waves are reported in Figs. 11–14, while the evolution of the indicators x_c and s is reported in Figs. 15 and 16. The plots in these figures are qualitatively very similar to those presented above. This suggests that, to observe different phenomena, the shape of the impulse must be changed.

To trigger different wave propagation phenomena, a further simple impulse was considered, namely the square wave impulse, see Fig. 5(right). Firstly, the case characterized by $\bar{p} = 1000$ N and $t_l = 0.005$ s was studied. Figs. 17 and 18 report some stroboscopic shoots for ε-, φ- and κ-waves. The evolution of the synthetic indicators x_c and s for ε-, φ- and κ-waves is reported in Fig. 19.

At first, it is worth to observe that applying a rectangular impulse is physically close to a *hammering*, while applying a square wave impulse is physically close to flicking. The noticeable differences with the results obtained in the previous

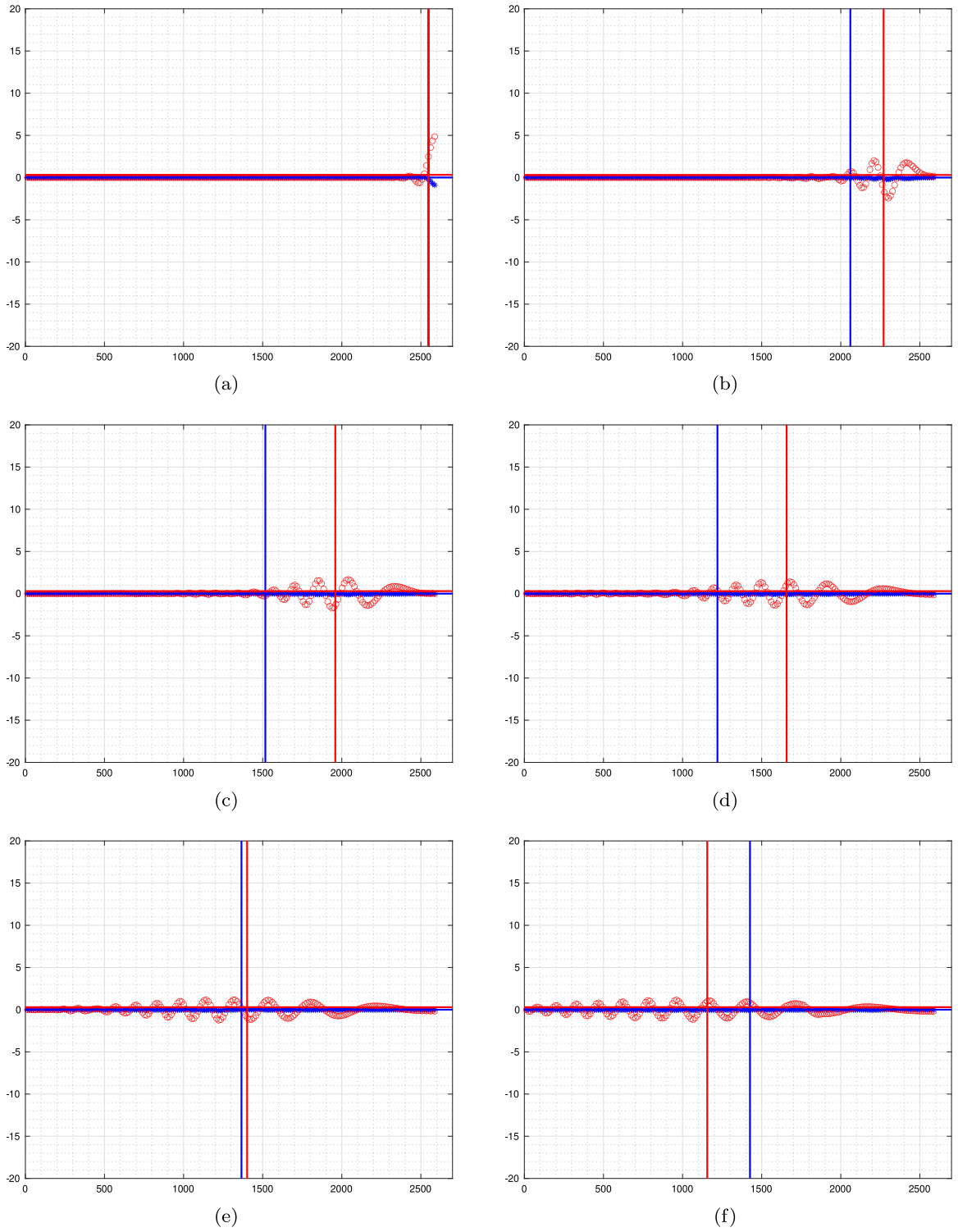

Fig. 17. Stroboscopic shoots illustrating the propagation of ε- and φ-waves for $t/\Delta t = 50$, 217, 384, 551, 718 and 885 for the case of the square wave impulse with $\bar{p} = 1000$ N and $t_l = 0.005$ s. The vertical and horizontal lines indicate, respectively, the centroid and the variance of the same-color wave at a given time instant. Blue and red colors are associated, respectively, with ε- and φ-waves. (For interpretation of the references to color in this figure legend, the reader is referred to the web version of this article.)

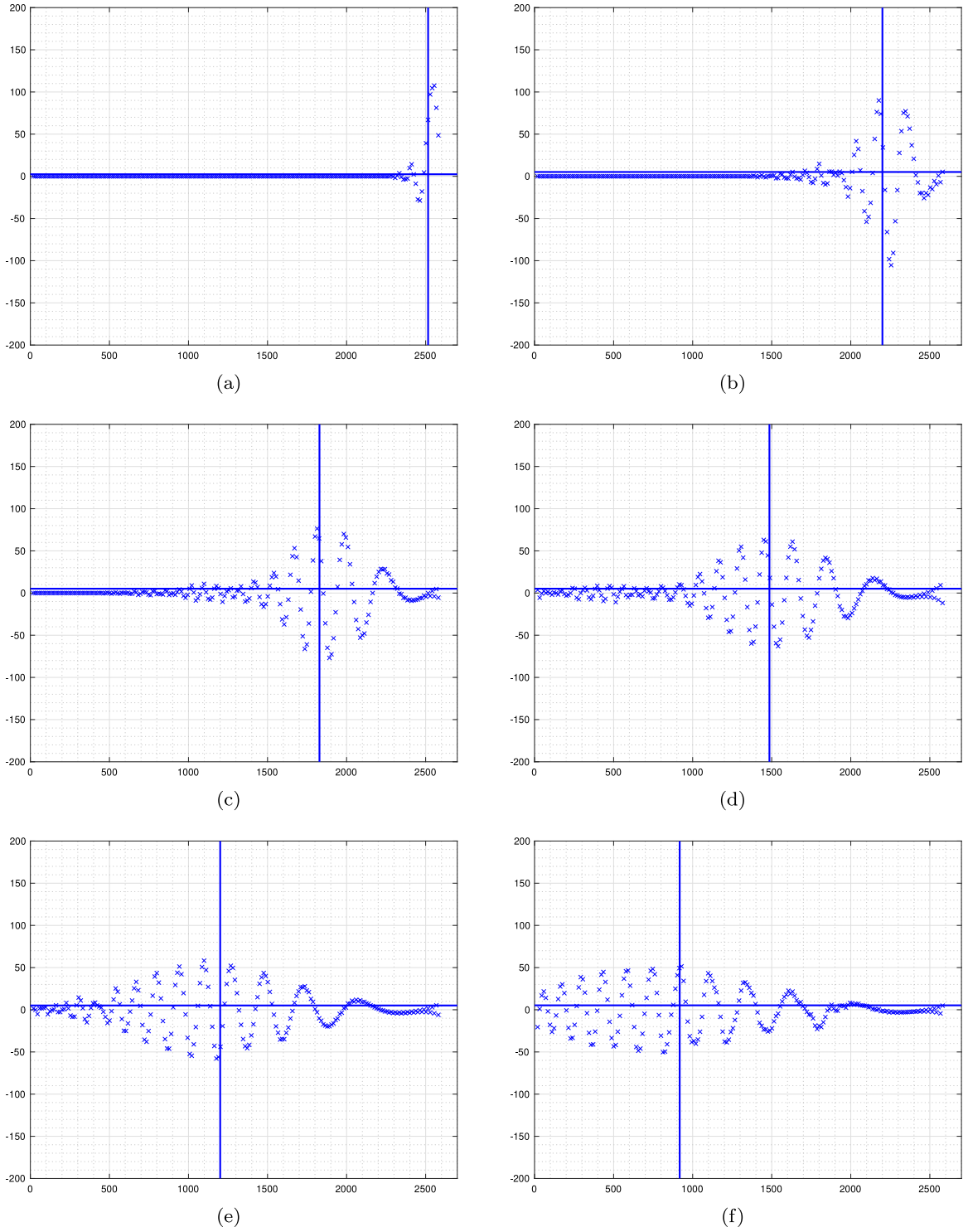

Fig. 18. Stroboscopic shoots illustrating the propagation of κ-waves for $t/\Delta t = 50$, 217, 384, 551, 718 and 885 for the case of the square wave impulse with $\bar{p} = 1000$ N and $t_l = 0.005$ s. The vertical and horizontal lines indicate, respectively, the centroid and the variance of the wave at a given time instant.

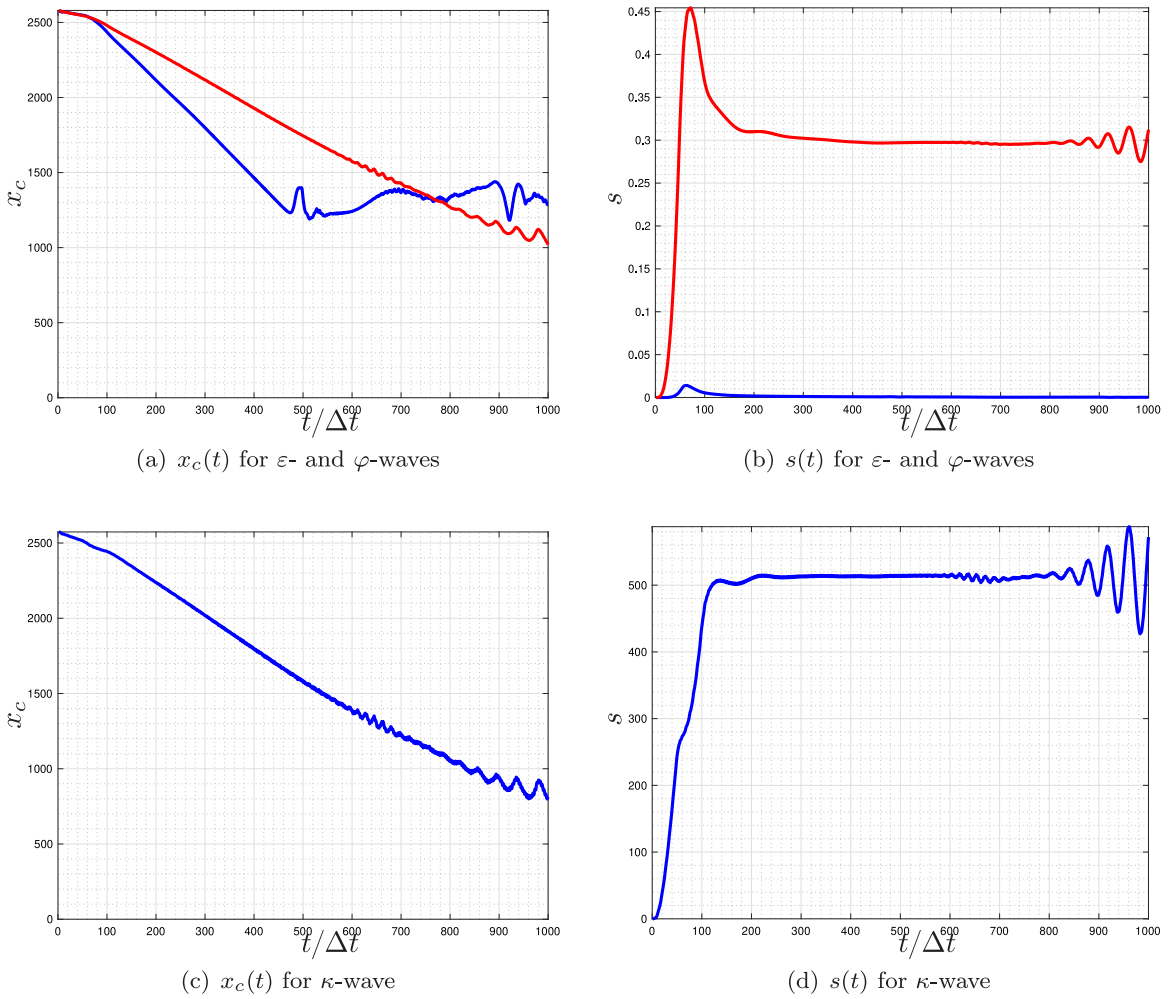

(a) $x_c(t)$ for ε- and φ-waves

(b) $s(t)$ for ε- and φ-waves

(c) $x_c(t)$ for κ-wave

(d) $s(t)$ for κ-wave

Fig. 19. Evolution of the centroid x_c and of the variance s for ε-, φ- and κ-waves in the case of the square wave impulse with $\bar{p} = 1000$ N and $t_l = 0.005$ s. In the plots (a) and (b), blue and red colors refer to ε- and φ-waves, respectively. (For interpretation of the references to color in this figure legend, the reader is referred to the web version of this article.)

cases is that the velocities of ε-, φ-, and κ-waves are much higher, which allows also to see clearly that a stationary state is reached for the variance of all waves and for the centroid position of ε-waves. Clearly, for symmetry reasons, the mean value of the centroid position of ε-waves after reflection, when the stationary state seems to be reached, is half the length of the beam. Using the same argument, it can be concluded that for the other wave types the steady state is not reached within the time horizon of the simulation. It is worth remarking that extremely high oscillations are observed for the κ-wave, which sometimes seems to have a *double tail*. For all types of wave, the formation of a wave packet can be seen neatly. Such a wave packet changes its shape, actually spreads around by increasing its support, while propagating, which is an indication of dispersion. This pushed us to perform the same parametric study done for the rectangular impulse also for the square wave impulse. The question that we asked ourselves is: for a fixed momentum entered from the external world into the system, what is the effect of changing the time-duration of the impulse?

To answer the previous question, we halved and then divided by four the parameter t_l considered before, doubling and quadruplicating the force $\bar{p}$, respectively. Figs. 20, 21, and 22 and Figs. 23, 24, and 25 report some stroboscopic shoots of ε-, φ-, and κ-waves, along with the evolution of the indicators x_c and s, for the cases $\bar{p} = 2000$ N and $t_l = 0.0025$ s and $\bar{p} = 4000$ N and $t_l = 0.00125$ s, respectively. It is remarkable that, the higher the quantity $\bar{p}$, the higher the values of the linearized discrete curvature of the center line of the pantographic beam. Additionally, it can be concluded that for higher values of $\bar{p}$, the stationary state of the variance of ε-, φ-, and κ-waves is affected by beatings. We remark that, on the one hand, the last considered time-support of the square wave impulse is sufficiently small to approach, in the selected time horizon, the stationary state, see the waves' centroids position in Fig. 25. On the other hand, the increased value of the magnitude of the impulse does not only induce higher waves' velocities, but also a neater and stronger reflection of the centroid of the extensional deformation of the center line.

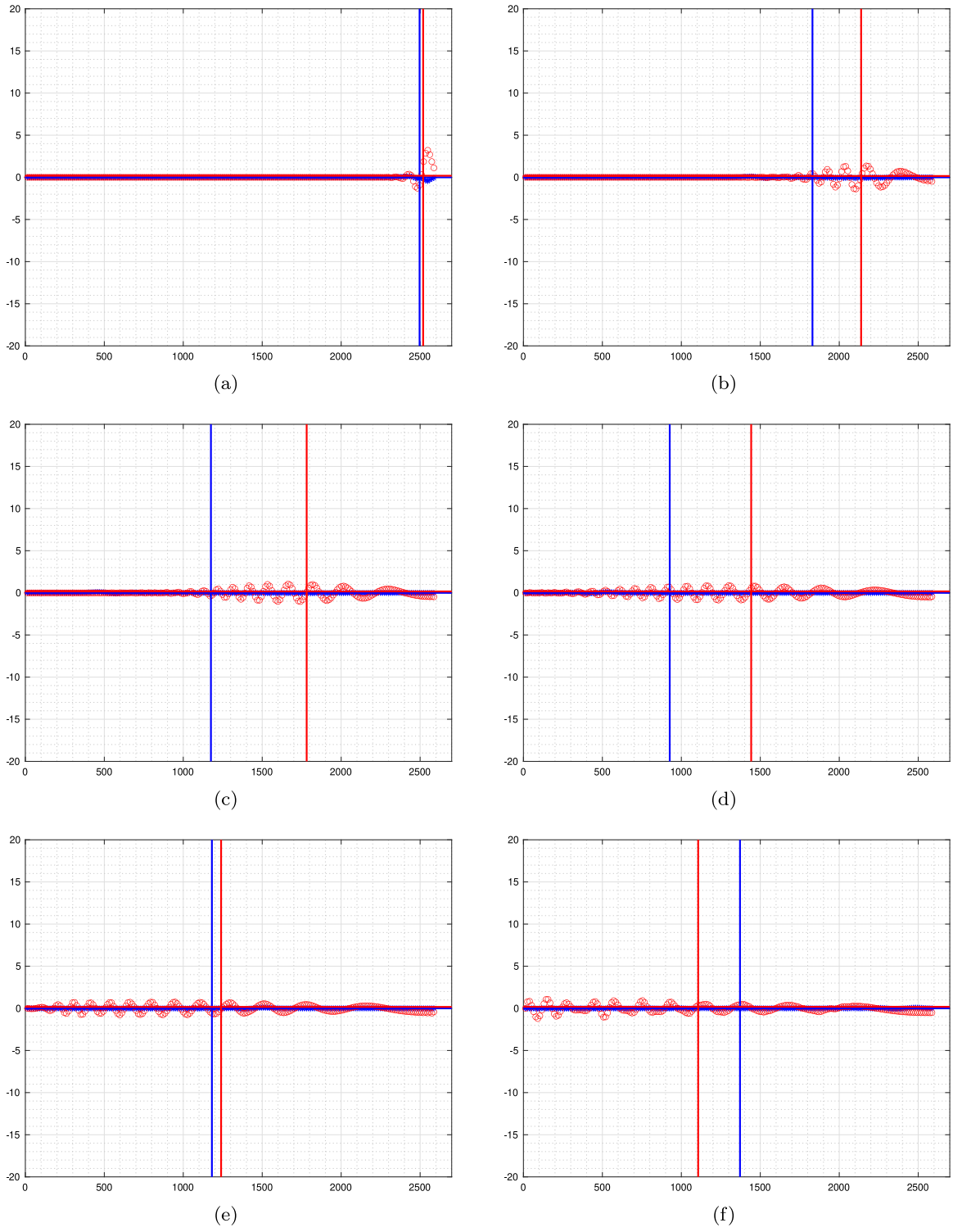

Fig. 20. Stroboscopic shoots illustrating the propagation of ε- and φ-waves for $t/\Delta t = 50$, 217, 384, 551, 718 and 885 for the case of the square wave impulse with $\bar{p} = 2000$ N and $t_l = 0.0025$ s. The vertical and horizontal lines indicate, respectively, the centroid and the variance of the same-color wave at a given time instant. Blue and red colors are associated, respectively, with $\varepsilon-$ and $\varphi-$waves. (For interpretation of the references to color in this figure legend, the reader is referred to the web version of this article.)

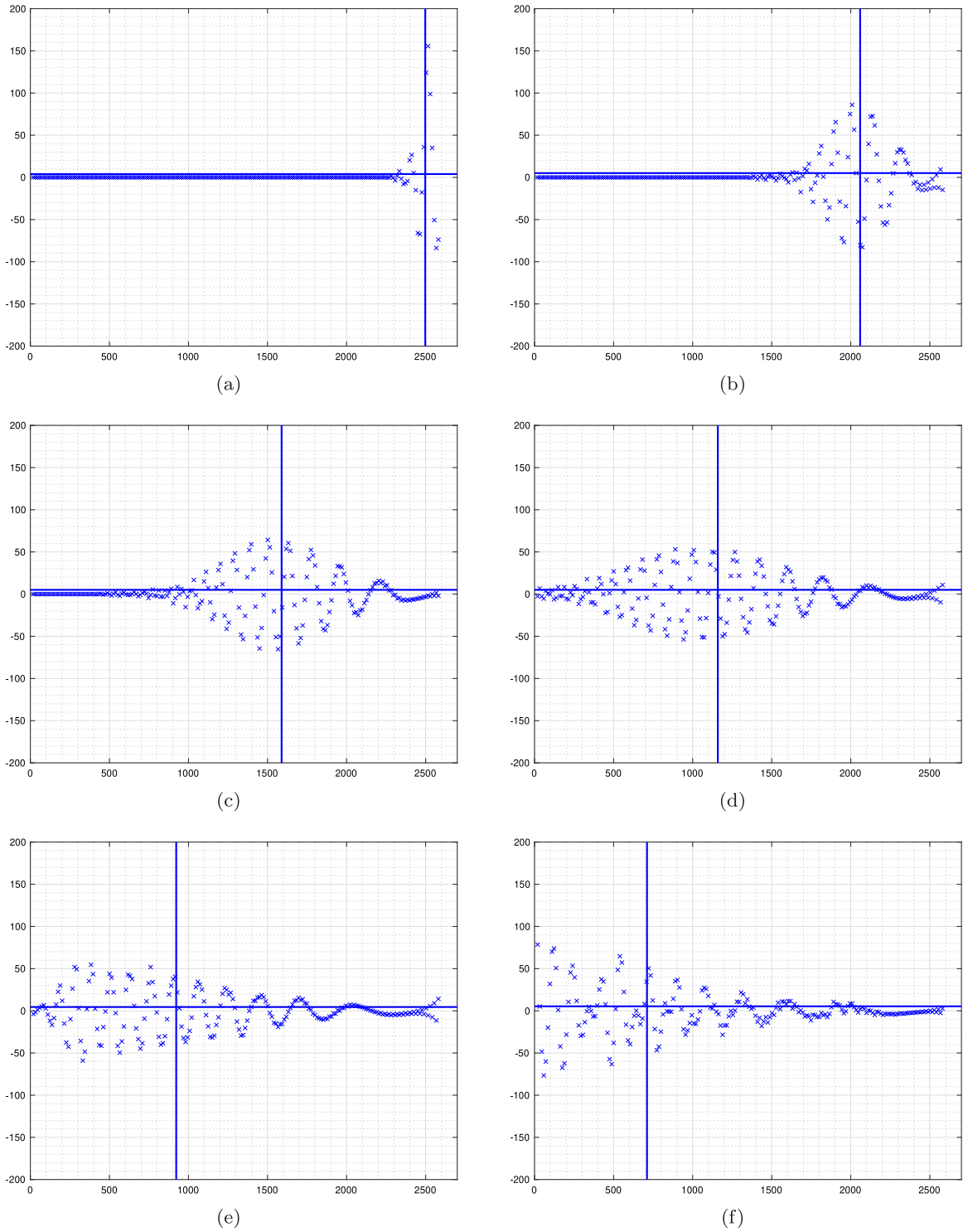

Fig. 21. Stroboscopic shoots illustrating the propagation of κ-waves for $t/\Delta t = 50$, 217, 384, 551, 718 and 885 for the case of the rectangular impulse with $\bar{p} = 2000$ N and $t_l = 0.0025$ s. The vertical and horizontal lines indicate, respectively, the centroid and the variance of the wave at a given time instant.

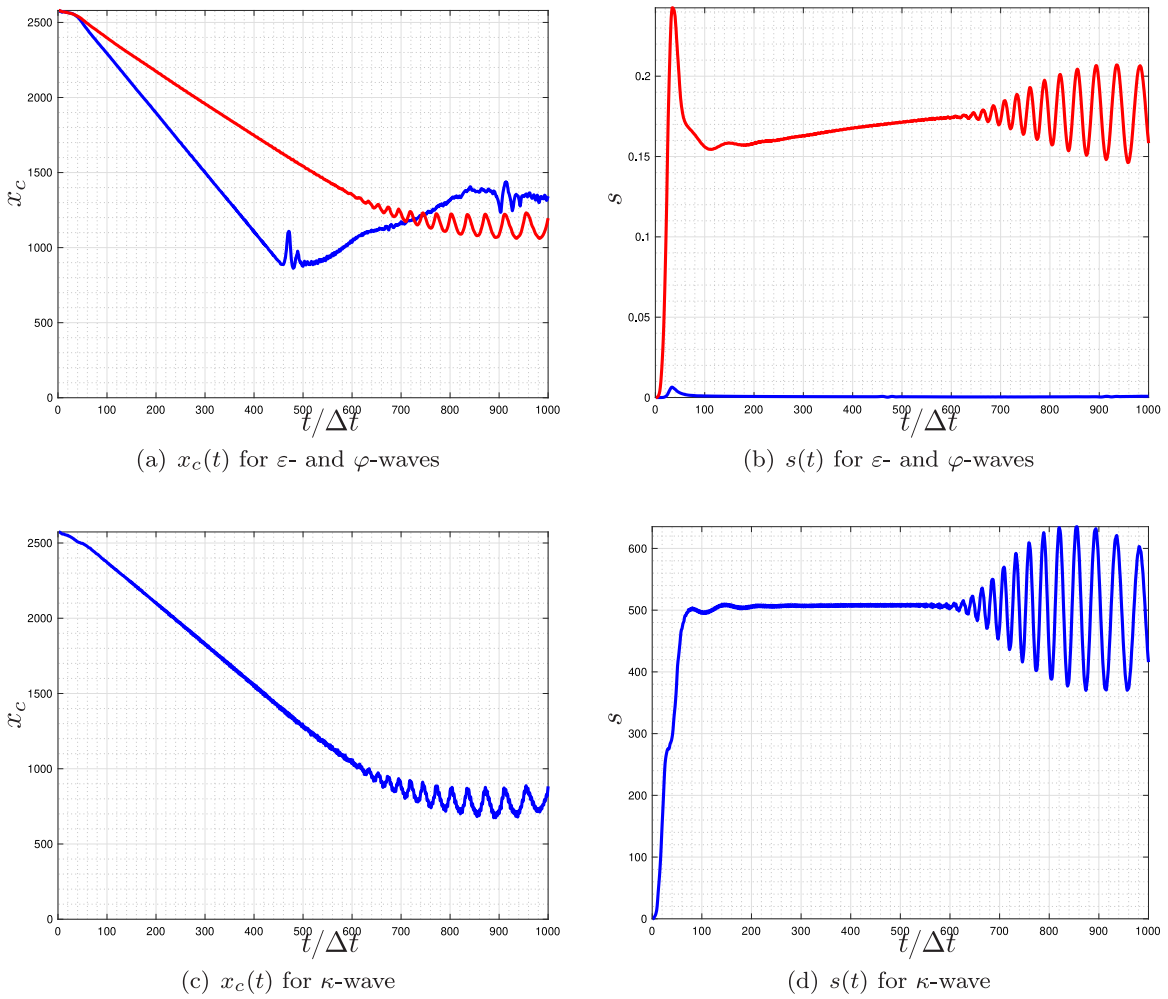

(a) $x_c(t)$ for ε- and φ-waves

(b) $s(t)$ for ε- and φ-waves

(c) $x_c(t)$ for κ-wave

(d) $s(t)$ for κ-wave

Fig. 22. Evolution of the centroid x_c and of the variance s for ε-, φ- and κ-waves in the case of the rectangular impulse with $\bar{p} = 2000$ N and $t_l = 0.0025$ s. In the plots (a) and (b), blue and red colors refer to ε- and φ-waves, respectively. (For interpretation of the references to color in this figure legend, the reader is referred to the web version of this article.)

5. Concluding remarks and future challenges

In the present study we have made use of discrete simulations to provide nodal trajectories in a discrete pantographic beam modeled by means of a mass–spring system. We addressed the large displacements regime by means of a time-stepping scheme that allowed us to reconstruct the motion. We defined new observable variables, such us the discrete extension, linearized relative rotation of the tangent, and linearized curvature of the center line, that proved to be more suitable than the displacement variables in studying wave propagation in pantographic beams. Due to the characteristic accordion-like deformation mode of pantographic beam, which is usually the most compliant one, displacement does not propagate in a wave-like manner as quick as strain waves, which instead are defined considering the relative motion of adjacent nodes along the center line of the pantographic beam. The considered boundary conditions consisted of a clamp condition at the left end of the pantographic beam and a free boundary condition at the right end of the beam. A transverse impulsive force has been applied at the free end. The features of strain waves, such as their variance and centroid, have been studied.

The study that we have conducted allows to conclude that: *(i)* nonlinear wave in pantographic beams, coupling axial and transverse motion, can be triggered by a transverse load with sufficiently high amplitude applied for a sufficiently long time; *(ii)* ε- and φ-waves travel at a different velocity than κ-waves and, due to their different nature, *i.e.* definition, these three types of wave interact differently with a constrained boundary; *(iii)* after reflection, strain waves reflected at the boundary sum up with incoming waves from the right end giving at stationary state a periodic strain wave or, at least, a strain wave oscillating around a periodic shape; *(iv)* the centroid position of a wave, as well as its variance, are two useful and meaningful synthetic quantities that tell us much about the features of wave propagation; *(v)* the

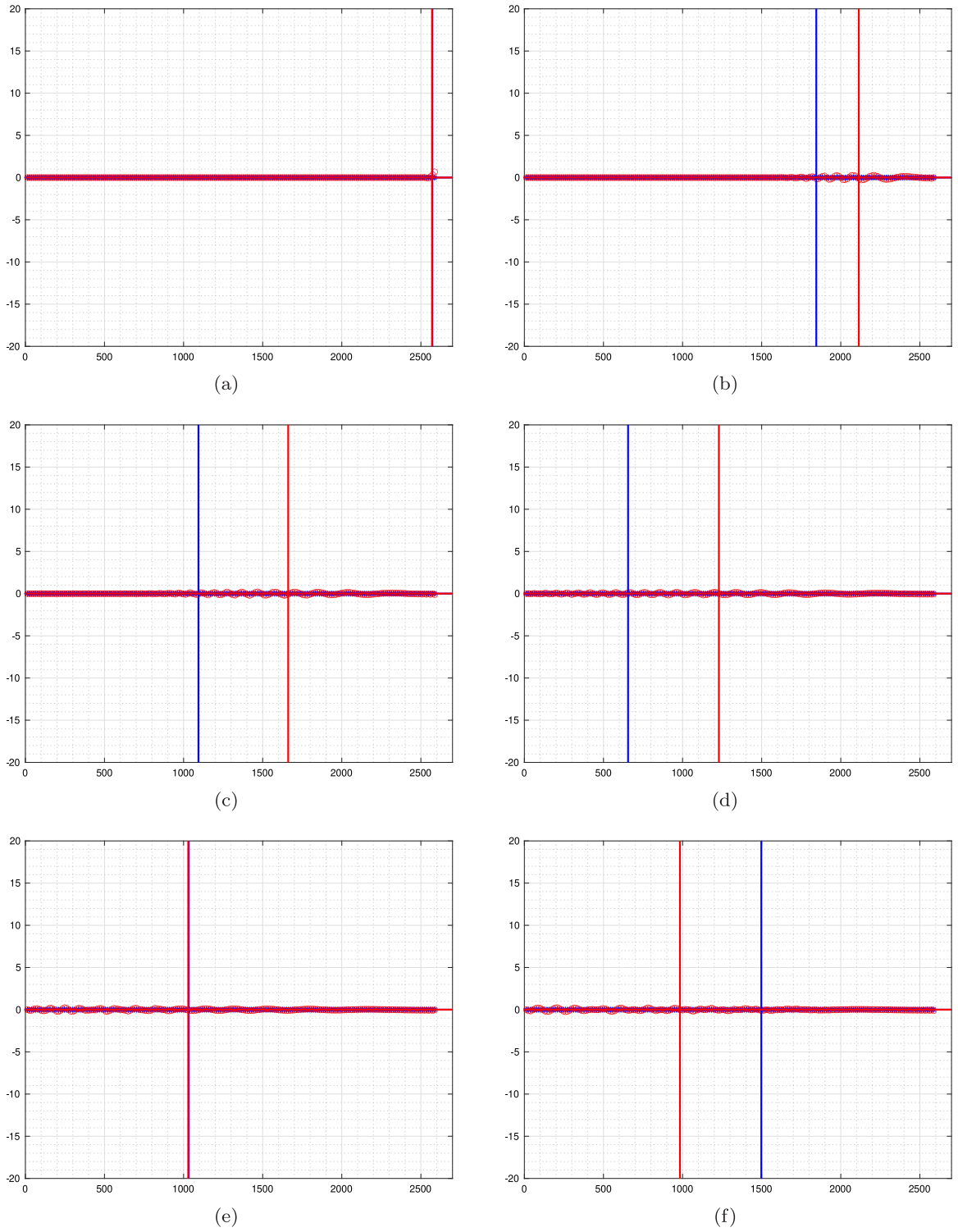

Fig. 23. Stroboscopic shoots illustrating the propagation of ε- and φ-waves for $t/\Delta t = 50$, 883, 1716, 2549, 3382 and 4215 for the case of the square wave impulse with $\bar{p} = 4000$ N and $t_l = 0.00125$ s. The vertical and horizontal lines indicate, respectively, the centroid and the variance of the same-color wave at a given time instant. Blue and red colors are associated, respectively, with ε- and φ-waves. (For interpretation of the references to color in this figure legend, the reader is referred to the web version of this article.)

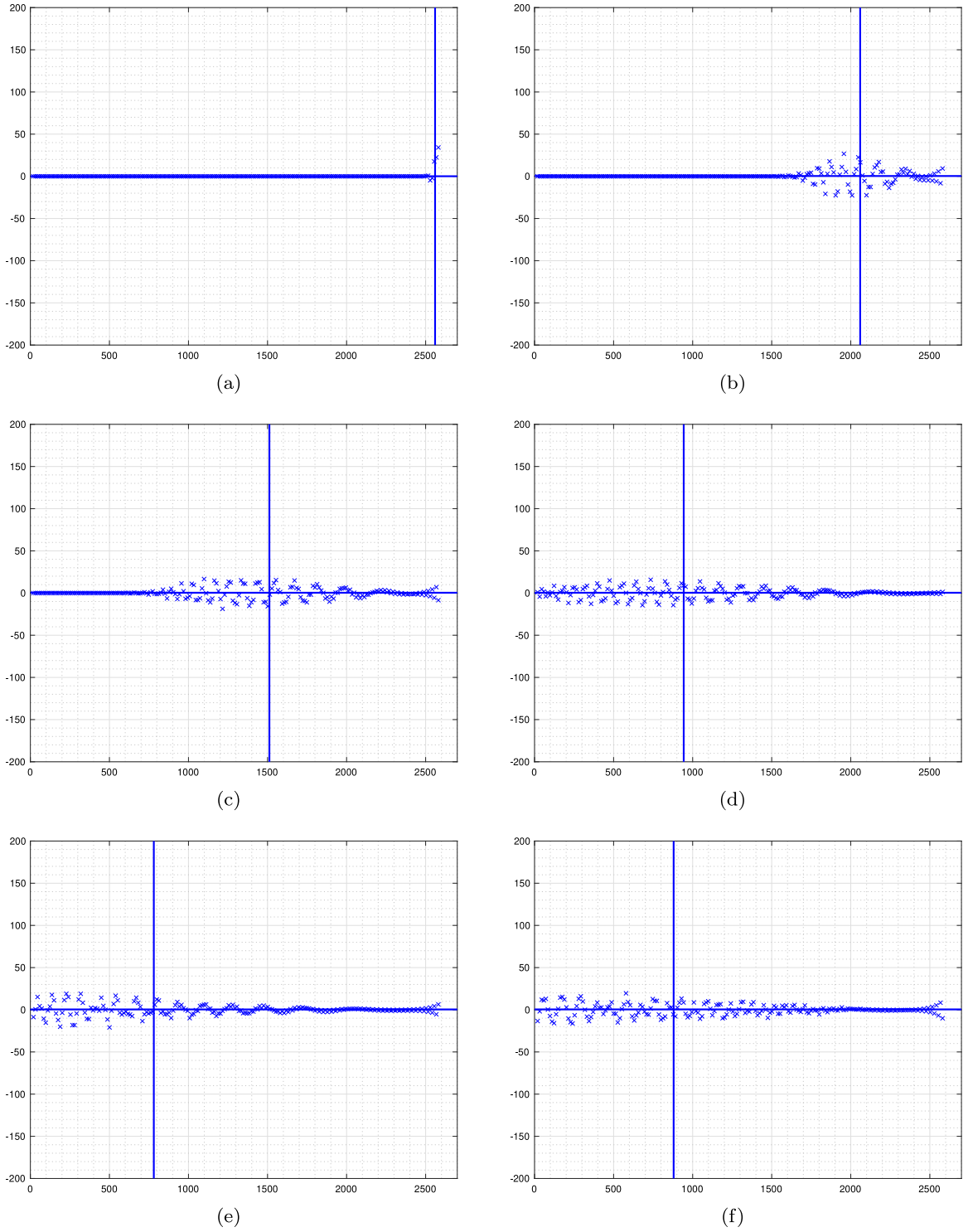

Fig. 24. Stroboscopic shoots illustrating the propagation of κ-waves for $t/\Delta t = 50$, 883, 1716, 2549, 3382 and 4215 for the case of the rectangular impulse with $\bar{p} = 4000$ N and $t_l = 0.00125$ s. The vertical and horizontal lines indicate, respectively, the centroid and the variance of the wave at a given time instant.

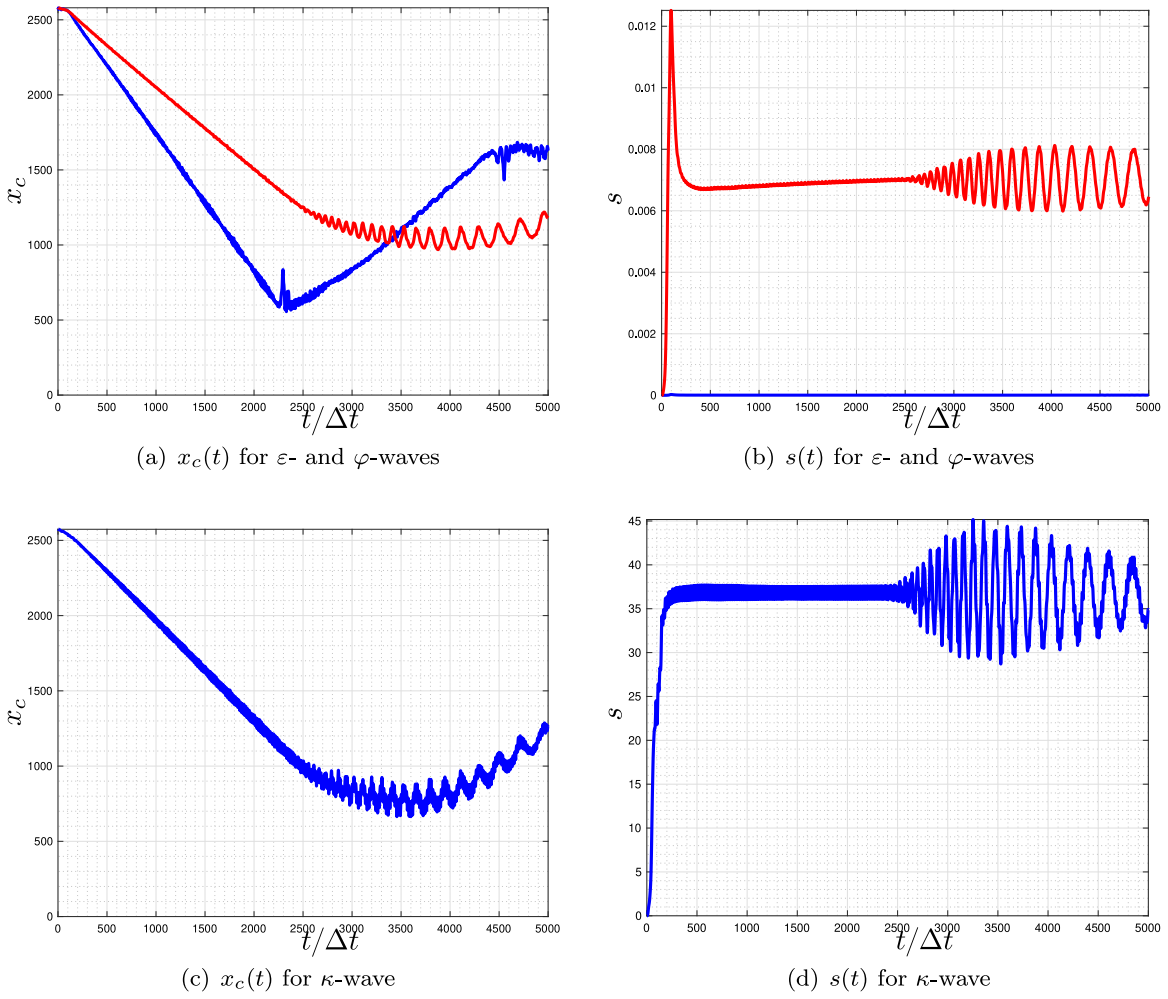

(a) $x_c(t)$ for ε- and φ-waves

(b) $s(t)$ for ε- and φ-waves

(c) $x_c(t)$ for κ-wave

(d) $s(t)$ for κ-wave

Fig. 25. Evolution of the centroid x_c and of the variance s for ε-, φ- and κ-waves in the case of the rectangular impulse with $\bar{p} = 4000$ N and $t_l = 0.00125$ s. In the plots (a) and (b), blue and red colors refer to ε- and φ-waves, respectively. (For interpretation of the references to color in this figure legend, the reader is referred to the web version of this article.)

advantage of using these quantities lies in the fact that they are purely kinematic in nature, namely they can be defined for any system in any regime; *(vi)* when the pantographic beam is subjected to flicking, strain wave packets, *i.e.* short *bursts* or *envelopes* of localized wave action that travels as a unit, are observed and it is seen that they change their shape while propagating and such a change is affected by the duration of the impulse, for a fixed momentum entered from the external world into the pantographic beam system; *(vii)* when the steady state, that for the centroid of the strain waves is the middle of the beam, is reached, oscillations of the centroid position and wave variance, even with multiple time-scales, are observed, including beating phenomena eventually; *(viii)* the centroid position, for all the strain waves, advances with constant velocity in time until the wave interacts with the left boundary, this is a remarkable property as it allows to define clearly a wave velocity.

Future challenges of the present work include the development of a more systematic way to change the features of the applied impulse in order to explore easily a wider parameter space, as well as the interpretation of the results obtained through the current analysis by making use of a homogenized continuum model. It is worth to remark in this regard that if analytical solutions are found for the continuum in terms of a family of displacement fields parameterized over time, they can be computed at the boundary, resulting in a nodal displacement as a function of time. The latter can be used together with constitutive relationships to compute the nodal force, that can be then in turn applied in the discrete system to compare the continuum and discrete wave propagation.

Declaration of competing interest

The authors declare the following financial interests/personal relationships which may be considered as potential competing interests: Emilio Turco reports financial support was provided by University of Sassari.

Acknowledgments

Emilio Turco gratefully acknowledges the support of the University of Sassari, Italy (Fondo di Ateneo per la ricerca 2020). This work was carried out under the auspices of the Gruppo Nazionale di Fisica Matematica (GNFM) of the Istituto Nazionale di Alta Matematica (INDAM).

References

[1] E. Turco, E. Barchiesi, F. dell'Isola, A numerical investigation on impulse-induced nonlinear longitudinal waves in pantographic beams, Math. Mech. Solids 27 (1) (2021) 22–48.
[2] L. Placidi, E. Barchiesi, E. Turco, N.L. Rizzi, A review on 2D models for the description of pantographic fabrics, Z. Angew. Math. Phys. 67 (121) (2016) 1–20.
[3] F. dell'Isola, P. Seppecher, J.J. Alibert, T. Lekszycki, R. Grygoruk, M. Pawlikowski, D.J. Steigmann, I. Giorgio, U. Andreaus, E. Turco, M. Gołaszewski, N. Rizzi, C. Boutin, V.A. Eremeyev, A. Misra, L. Placidi, E. Barchiesi, L. Greco, M. Cuomo, A. Cazzani, A. Della Corte, A. Battista, D. Scerrato, I. Zurba Eremeeva, Y. Rahali, J.-F. Ganghoffer, W. Muller, G. Ganzosch, M. Spagnuolo, A. Pfaff, K. Barcz, K. Hoschke, J. Neggers, F. Hild, Pantographic metamaterials: an example of mathematically driven design and of its technological challenges, Contin. Mech. Thermodyn. 31 (4) (2019) 851–884.
[4] F. Hild, A. Misra, F. dell'Isola, Multiscale DIC applied to pantographic structures. Experimental mechanics, Exp. Mech. 61 (2) (2021) 431–443.
[5] M. Spagnuolo, U. Andreaus, A. Misra, I. Giorgio, F. Hild, Mesoscale modeling and experimental analyses for pantographic cells: effect of hinge deformation, Mech. Mater. 160 (2021) 103924.
[6] I. Giorgio, Numerical identification procedure between a micro Cauchy model and a macro second gradient model for planar pantographic structures, Z. Angew. Math. Mech. 67 (95) (2016) 1–17.
[7] H. Yang, G. Ganzosch, I. Giorgio, B.E. Abali, Material characterization and computations of a polymeric metamaterial with a pantographic substructure, Z. Angew. Math. Phys. 69 (4) (2018) 105.
[8] I. Giorgio, N.L. Rizzi, E. Turco, Continuum modelling of pantographic sheets for out-of-plane bifurcation and vibrational analysis, Proc. R. Soc. A: Math., Phys. Eng. Sci. 473 (2207) (2017) 1–21.
[9] I. Giorgio, D. Del Vescovo, Energy-based trajectory tracking and vibration control for multi-link highly flexible manipulators, Math. Mech. Complex Syst. 7 (2) (2019) 159–174.
[10] M. Spagnuolo, P. Peyre, C. Dupuy, Phenomenological aspects of quasi-perfect pivots in metallic pantographic structures, Mech. Res. Commun. 101 (2019) 103415.
[11] M. Golaszewski, R. Grygoruk, I. Giorgio, M. Laudato, F. di Cosmo, Metamaterials with relative displacements in their microstructure: technological challenges in 3D printing, experiments and numerical predictions, Contin. Mech. Thermodyn. 31 (4) (2019) 1015–1034.
[12] E. Turco, M. Golaszewski, I. Giorgio, F. D'Annibale, Pantographic lattices with non-orthogonal fibres: experiments and their numerical simulations, Composites Part B: Eng. 118 (2017) 1–14.
[13] D. Scerrato, I. Giorgio, N.L. Rizzi, Three-dimensional instabilities of pantographic sheets with parabolic lattices: numerical investigations, ZAMM - J. Appl. Math. Mech. / Z. Angew. Math. Mech. 67 (53) (2016) 1–19.
[14] F. dell'Isola, P. Seppecher, M. Spagnuolo, E. Barchiesi, F. Hild, T. Lekszycki, I. Giorgio, L. Placidi, U. Andreaus, M. Cuomo, S.R. Eugster, A. Pfaff, K. Hoschke, R. Langkemper, E. Turco, R. Sarikaya, A. Misra, M. De Angelo, F. D'Annibale, A. Bouterf, X. Pinelli, A. Misra, B. Desmorat, M. Pawlikowski, C. Dupuy, D. Scerrato, P. Peyre, M. Laudato, L. Manzari, P. Göransson, C. Hesch, S. Hesch, P. Franciosi, J. Dirrenberger, F. Maurin, Z. Vangelatos, C. Grigoropoulos, V. Melissinaki, M. Farsari, W. Muller, B. Emek Abali, C. Liebold, G. Ganzosch, P. Harrison, R. Drobnicki, L. Igumnov, F. Alzahrani, T. Hayat, Advances in pantographic structures: design, manufacturing, models, experiments and image analyses, Contin. Mech. Thermodyn. 31 (4) (2019) 1231–1282.
[15] A. Juritza, H. Yang, G. Ganzosch, Qualitative Investigations of Experiments Performed on 3D-FDM-Printed Pantographic Structures Made Out of PLA, Springer International Publishing, Cham, 2019, pp. 197–209.
[16] A. Trippel, M. Stilz, F. Gutmann, G.C. Ganzenmueller, S. Hiermaier, A device for characterizing rotational joints in metamaterials, Mech. Res. Commun. 104 (2020) 103501.
[17] N. Nejadsadeghi, M. Laudato, M. De Angelo, A. Misra, Mechanical Behavior Investigation of 3D Printed Pantographic Unit Cells Via Tension and Compression Tests, Springer International Publishing, Cham, 2020, pp. 409–422.
[18] F. dell'Isola, E. Turco, A. Misra, Z. Vangelatos, C. Grigoropoulos, V. Melissinaki, M. Farsari, Force–displacement relationship in micro-metric pantographs: experiments and numerical simulations, C. R. - Méc. 347 (5) (2019) 397–405.
[19] Z. Vangelatos, M.E. Yildzdag, I. Giorgio, F. dell'Isola, C. Grigoropoulos, Investigating the mechanical response of microscale pantographic structures fabricated by multiphoton lithography, Extreme Mech. Lett. 43 (2021) 101202.
[20] E. Barchiesi, S.R. Eugster, L. Placidi, F. dell'Isola, Pantographic beam: A complete second gradient 1D-continuum in plane, Z. Angew. Math. Phys. 70 (135) (2019).
[21] E. Barchiesi, M. Laudato, F. Di Cosmo, Wave dispersion in non-linear pantographic beams, Mech. Res. Commun. 94 (2018) 128–132.
[22] E. Turco, E. Barchiesi, Equilibrium paths of Hencky pantographic beams in a three-point bending problem, Math. Mech. Complex Syst. 7 (4) (2019) 287–310.
[23] E. Turco, Stepwise analysis of pantographic beams subjected to impulsive loads, Math. Mech. Solids (2020) 1–18, http://dx.doi.org/10.1177/1081286520938841.
[24] I. Giorgio, F. dell'Isola, A. Misra, Chirality in 2D cosserat media related to stretch-micro-rotation coupling with links to granular micromechanics, Int. J. Solids Struct. 202 (2020) 28–38.
[25] A. Misra, N. Nejadsadeghi, M. De Angelo, L. Placidi, Chiral metamaterial predicted by granular micromechanics: verified with 1D example synthesized using additive manufacturing, Contin. Mech. Thermodyn. (2020) 1–17, http://dx.doi.org/10.1007/s00161-020-00862-8.
[26] M. De Angelo, L. Placidi, N. Nejadsadeghi, A. Misra, Non-standard timoshenko beam model for chiral metamaterial: identification of stiffness parameters, Mech. Res. Commun. 103 (103462) (2020) 1–8.
[27] I. Fernandez-Corbaton, C. Rockstuhl, P. Ziemke, P. Gumbsch, A. Albiez, R. Schwaiger, T. Frenzel, M. Kadic, M. Wegener, New twists of 3D chiral metamaterials, Adv. Mater. 31 (26) (2019) 1807742.
[28] Y.Y. Chen, G.L. Huang, C.T. Sun, Band gap control in an active elastic metamaterial with negative capacitance piezoelectric shunting, J. Vib. Acoust. 136 (6) (2014) 061008, 09.
[29] A. Madeo, G. Barbagallo, M.V. d'Agostino, L. Placidi, Patrizio Neff, First evidence of non-locality in real band-gap metamaterials: determining parameters in the relaxed micromorphic model, Proc. R. Soc. A: Math., Phys. Eng. Sci. 472 (20160169) (2016) 1–21.
[30] M.G. El Sherbiny, L. Placidi, Discrete and continuous aspects of some metamaterial elastic structures with band gaps, Arch. Appl. Mech. 88 (2018) 1725–1742.

[31] Y. Wang, O. Sigmund, Quasiperiodic mechanical metamaterials with extreme isotropic stiffness, Extreme Mech. Lett. 34 (2020) 100596.
[32] M. Kadic, T. Bückmann, R. Schittny, M. Wegener, On anisotropic versions of three-dimensional pentamode metamaterials, New J. Phys. 15 (2) (2013) 023029.
[33] M.J. Mirzaali, R. Hedayati, P. Vena, L. Vergani, M. Strano, A.A. Zadpoor, Rational design of soft mechanical metamaterials: Independent tailoring of elastic properties with randomness, Appl. Phys. Lett. 111 (5) (2017) 051903.
[34] E. Barchiesi, S.R. Eugster, F. dell'Isola, F. Hild, Large in-plane elastic deformations of bi-pantographic fabrics: asymptotic homogenization and experimental validation, Math. Mech. Solids 25 (3) (2020) 739–767.
[35] E. Turco, M. Golaszewski, A. Cazzani, N.L. Rizzi, Large deformations induced in planar pantographic sheets by loads applied on fibers: experimental validation of a discrete Lagrangian model, Mech. Res. Commun. 76 (2016) 51–56.
[36] Z. Vangelatos, V. Melissinaki, M. Farsari, K. Komvopoulos, C. Grigoropoulos, Intertwined microlattices greatly enhance the performance of mechanical metamaterials, Math. Mech. Solids 24 (8) (2019) 2636–2648.
[37] Z. Vangelatos, G.X. Gu, C.P. Grigoropoulos, Architected metamaterials with tailored 3D buckling mechanisms at the microscale, Extreme Mech. Lett. 33 (2019) 100580.
[38] E. Barchiesi, F. dell'Isola, A.M. Bersani, E. Turco, Equilibria determination of elastic articulated duoskelion beams in 2D via a riks-type algorithm, Int. J. Non-Linear Mech. 128 (103628) (2021) 1–24.
[39] E. Turco, Modeling of three-dimensional beam nonlinear vibrations generalizing hencky's ideas, Math. Mech. Solids 27 (10) (2022) 1950–1973.
[40] E. Barchiesi, M. Spagnuolo, L. Placidi, Mechanical metamaterials: A state of the art, Math. Mech. Solids 24 (1) (2019) 212–234.
[41] V.A. Eremeyev, J.F. Ganghoffer, V. Konopińska-Zmysłowska, N.S. Uglov, Flexoelectricity and apparent piezoelectricity of a pantographic micro-bar, Int. J. Eng. Sci. 149 (2020) 103213.
[42] T. Djourachkovitch, N. Blal, N. Hamila, A. Gravouil, Multiscale topology optimization of 3d structures: A micro-architectured materials database assisted strategy, Comput. Struct. 255 (2021) 106574.
[43] H. Abdoul-Anziz, P. Seppecher, Strain gradient and generalized continua obtained by homogenizing frame lattices, Math. Mech. Complex Syst. 6 (3) (2018) 213–250.
[44] R.D. Mindlin, Micro-structure in linear elasticity, Arch. Ration. Mech. Anal. 16 (1) (1964) 51–78.
[45] F. dell'Isola, A. Della Corte, I. Giorgio, Higher gradient continua: the legacy of piola, mindlin, sedov and toupin and some future research perspectives, Math. Mech. Solids 22 (4) (2017) 852–872.
[46] F. dell'Isola, U. Andreaus, L. Placidi, At the origins and in the vanguard of peridynamics, non-local and higher-gradient continuum mechanics: An underestimated and still topical contribution of Gabrio Piola, Math. Mech. Solids 20 (8) (2015) 887–928.
[47] B. Durand, A. Lebée, P. Seppecher, K. Sab, Predictive strain-gradient homogenization of a pantographic material with compliant junctions, J. Mech. Phys. Solids 160 (2022) 104773.
[48] E. Turco, A. Misra, M. Pawlikowski, F. dell'Isola, F. Hild, Enhanced Piola–Hencky discrete models for pantographic sheets with pivots without deformation energy: numerics and experiments, Int. J. Solids Struct. 147 (2018) 94–109.
[49] U. Andreaus, M. Spagnuolo, T. Lekszycki, S.R. Eugster, A Ritz approach for the static analysis of planar pantographic structures modeled with nonlinear Euler–Bernoulli beams, Contin. Mech. Thermodyn. 30 (2018) 1103–1123.
[50] V.A. Eremeyev, W. Pietraszkiewicz, Material symmetry group and constitutive equations of micropolar anisotropic elastic solids, Math. Mech. Solids 21 (2) (2016) 210–221.
[51] V.A. Eremeyev, L.P. Lebedev, M.J. Cloud, On weak solutions of boundary value problems within the surface elasticity of *n*th order, ZAMM - J. Appl. Math. Mech. / Z. Angew. Math. Mech. 101 (3) (2021) e202000378.
[52] V.A. Eremeyev, F. dell'Isola, On weak solutions of the boundary value problem within linear dilatational strain gradient elasticity for polyhedral lipschitz domains, Math. Mech. Solids 27 (3) (2022) 433–445.
[53] V.A. Eremeyev, F. dell'Isola, C. Boutin, D. Steigmann, Linear pantographic sheets: Existence and uniqueness of weak solutions, J. Elast. 132 (2) (2018) 175–196.
[54] V.A. Eremeyev, F.S. Alzahrani, A. Cazzani, F. dell'Isola, T. Hayat, E. Turco, V. Konopińska-Zmysłowska, On existence and uniqueness of weak solutions for linear pantographic beam lattices models, Contin. Mech. Thermodyn. 31 (6) (2019) 1843–1861.
[55] E. Barchiesi, A. Misra, L. Placidi, E. Turco, Granular micromechanics-based identification of isotropic strain gradient parameters for elastic geometrically nonlinear deformations, ZAMM - Z. Angew. Math. Mech. (2021) 1–21, http://dx.doi.org/10.1002/zamm.202100059.
[56] L. Placidi, U. Andreaus, I. Giorgio, Identification of two-dimensional pantographic structure via a linear D4 orthotropic second gradient elastic model, J. Eng. Math. 103 (1) (2017) 1–21.
[57] N. Shekarchizadeh, B.E. Abali, E. Barchiesi, A.M. Bersani, Inverse analysis of metamaterials and parameter determination by means of an automatized optimization problem, ZAMM - J. Appl. Math. Mech. / Z. Angew. Math. Mech. 101 (8) (2021) e202000277.
[58] B.E. Abali, W.H. Müller, V.A. Eremeyev, Strain gradient elasticity with geometric nonlinearities and its computational evaluation, Mech. Adv. Mater. Mod. Process. 1 (4) (2015) 1–11.
[59] B.E. Abali, W.H. Müller, F. dell'Isola, Theory and computation of higher gradient elasticity theories based on action principles, Arch. Appl. Mech. 87 (9) (2017) 1495–1510.
[60] E. Turco, K. Barcz, M. Pawlikowski, N.L. Rizzi, Non-standard coupled extensional and bending bias tests for planar pantographic lattices. Part I: numerical simulations, Z. Angew. Math. Phys. 67 (122) (2016) 1–16.
[61] E. Turco, K. Barcz, N.L. Rizzi, Non-standard coupled extensional and bending bias tests for planar pantographic lattices. Part II: comparison with experimental evidence, Z. Angew. Math. Phys. 67 (123) (2016) 1–16.
[62] E. Turco, N.L. Rizzi, Pantographic structures presenting statistically distributed defects: numerical investigations of the effects on deformation fields, Mech. Res. Commun. 77 (2016) 65–69.
[63] E. Turco, Numerically driven tuning of equilibrium paths for pantographic beams, Contin. Mech. Thermodyn. 31 (2019) 1941–1960.
[64] S.R. Eugster, J. Harsch, A variational formulation of classical nonlinear beam theories, in: B.E. Abali, I. Giorgio (Eds.), Developments and Novel Approaches in Nonlinear Solid Body Mechanics, Springer, 2020, pp. 95–121.
[65] J. Harsch, S.R. Eugster, Finite element analysis of planar nonlinear classical beam theories, in: B.E. Abali, I. Giorgio (Eds.), Developments and Novel Approaches in Nonlinear Solid Body Mechanics, Springer, 2020, pp. 123–157.
[66] G. Capobianco, S.R. Eugster, T. Winandy, Modeling planar pantographic sheets using a nonlinear Euler–Bernoulli beam element based on B-spline functions, Proc. Appl. Math. Mech. 18 (1) (2018) 1–2.
[67] E. Turco, E. Barchiesi, I. Giorgio, F. dell'Isola, A Lagrangian hencky-type non-linear model suitable for metamaterials design of shearable and extensible slender deformable bodies alternative to timoshenko theory, Int. J. Non-Linear Mech. 123 (2020) 103481.
[68] E. Turco, F. dell'Isola, A. Cazzani, N.L. Rizzi, Hencky-type discrete model for pantographic structures: numerical comparison with second gradient continuum models, Z. Angew. Math. Phys. 67 (85) (2016) 1–28.
[69] E. Barchiesi, F. dell'Isola, M. Laudato, P. Seppecher, Advances in of microstructured media and structures, in: Chapter a 1D Continuum Model for Beams with Pantographic Microstructure: Asymptotic Micro-Macro Identification and Numerical Results, Springer, Cham, 2018, pp. 43–74.
[70] B. Desmorat, M. Spagnuolo, E. Turco, Stiffness optimization in nonlinear pantographic structures, Math. Mech. Solids 25 (11) (2020) 2252–2262.

[71] F. dell'Isola, D. Steigmann, A. Della Corte, E. Barchiesi, M. Laudato, F. Di Cosmo, M. Spagnuolo, I. Giorgio, P. Seppecher, A. Misra, E. Turco, T. Lekszycki, P. Peyre, C. Dupuy, F. Hild, J. Dirrenberger, U. Andreaus, L. Placidi, Discrete and Continuum Models for Complex Metamaterials, Cambridge University Press, 2020.
[72] P. Wriggers, Nonlinear Finite Element Methods, Springer, 2008.
[73] J.T. Katsikadelis, A new direct time integration method for the equations of motion in structural dynamics, ZAMM - J. Appl. Math. Mech. / Z. Angew. Math. Mech. 94 (9) (2013) 757–774.
[74] S. de Miranda, M. Mancuso, F. Ubertini, Time discontinuous Galerkin methods with energy decaying correction for non-linear elastodynamics, Int. J. Numer. Methods Eng. 83 (2010) 323–347.
[75] K.-J. Bathe, G. Noh, Insight into an implicit time integration scheme for structural dynamics, Comput. Struct. 98–99 (2012) 1–6.
[76] R. Casciaro, Time evolutional analysis of nonlinear structures, Meccanica 3 (X) (1975) 156–167.
[77] M. Aristodemo, A high-continuity finite element model for two-dimensional elastic problems, Comput. Struct. 21 (5) (1985) 987–993.
[78] E. Hewitt, R.E. Hewitt, The gibbs–wilbraham phenomenon: An episode in Fourier analysis, Arch. Hist. Exact Sci. 21 (2) (1979) 129–160.